JOURNAL OF GUIDANCE, CONTROL, AND DYNAMICS
Vol. 45, No. 2, February 2022

Pose Tracking Control for Spacecraft Proximity Operations Using the Udwadia–Kalaba Framework

Abin Alex Pothen,* Alexander Crain,† and Steve Ulrich‡
Carleton University, Ottawa, Ontario K1S 5B6, Canada

https://doi.org/10.2514/1.G005169

This paper develops an analytical dynamics-based approach for simultaneous position and orientation tracking control of a chaser spacecraft with respect to an uncontrolled target. The control requirements are formulated as holonomic or nonholonomic constraints, which are expressed as linear and angular acceleration constraints. The complete six-degree-of-freedom formulation of the Udwadia–Kalaba-based pose tracking controller generating exact real-time control forces and torques is presented. For design purposes, the method assumes a precise knowledge of the system parameters and states, along with perfect control action by the actuators. The exponential convergence of the constraint dynamics is proven using the Lyapunov stability theory. Simulation results demonstrate exponentially stable position and orientation tracking for close-proximity operations in perturbed low Earth orbits. Finally, the controller is experimentally validated using the Spacecraft Proximity Operations Testbed at Carleton University.

Downloaded by CARLETON UNIVERSITY on January 23, 2022 | http://arc.aiaa.org | DOI: 10.2514/1.G005169

I. Introduction

THE growing interest in space-based technology has resulted in overcrowding both active and nonactive satellites in lower Earth orbit, and removal of the nonactive debris has been proposed to maintain sustainability of the space environment. Active debris removal[§] and in-space refueling[¶] techniques are becoming potential solutions to manage the issue. However, enabling these techniques requires simultaneous and accurate tracking of both the relative translational and rotational motion of a chaser spacecraft with respect to a tumbling target object. This task is typically referred to as the pose tracking control problem.

The majority of techniques developed for real-time motion planning for moving target assume a point mass target [1–8]. Motion synchronization with a drifting and tumbling object is highly complex due to the requirement for precise control of the coupled translation and rotational motion in the final approach phase. Additionally, the low-frequency coupling between the relative target and chaser motion arising from orbital mechanics needs to be accounted for in the control design. To reduce the approach phase transient errors, notable multivariable strategies have been developed. For example, in operational scenarios, cross-coupling is feed-forward and combined with either a linear proportional-integral-derivative (PID) or a robust H_∞ feedback loop [9]. Ma et al. [10] formulated and analyzed the rendezvous control problem of a chaser spacecraft for optimal approach and alignment with a rotating target. They proposed an iterative algorithm for a planar case to solve the optimal trajectory with minimum time/fuel consumption, but the iterative nature of the solution increased the computational cost. An experimental study of close-range rendezvous and docking for a cooperative target was presented by Romano et al. [11]. However, the target spacecraft was assumed to be active and capable of attitude stabilization using on-board thrusters while the chaser is docking to it. Zhang et al. [12] used artificial potential functions for rendezvous and docking guidance to capture a non-cooperative target in the presence of static and dynamic obstacles. This method suffered from the well-known local minima issue associated with potential functions closer to obstacles. The Canadian Space Agency developed a combined prediction and motion-planning strategy for docking with a drifting and tumbling target [13]. The problem of finding the optimal rendezvous point to null out the relative motion was presented as solving the system Hamiltonian function for the terminal time by using a Newton–Raphson numerical technique. However, the numerical solution of the nonlinear optimization problem prevented autonomous, real-time application of this technique on a flight computer. More recently, Wilde et al. [14] experimentally demonstrated inverse dynamics-based trajectory optimization for planar docking of a chaser to an uncontrolled spinning object, though the rigid target was assumed to be spinning along a single axis without translating. Ventura et al. [15] presented a spatial inverse-dynamics-based approach for docking to a tumbling object where the inversion for the iterative generation of optimal trajectories was done in a virtual domain rather than a time domain. The approach trajectory was calculated and the control updated using the current state estimates. Zagaris and Romano [16] proposed a reachability analysis for planar docking to a spinning target. The translational-only control problem of rendezvous and docking was addressed by Dong et al. [17] encoding the approach and obstacle avoidance constraints into the artificial potential function and sliding mode scheme, after which an adaptive controller was implemented. However, full six-degree-of-freedom (6-DOF) control of both the translational and rotational motion is required to achieve precise pose tracking in space.

Using the Euler–Lagrange approach, Kristiansen et al. [18] compared passivity-based proportional-derivative control, sliding mode control, and integrator backstepping to address 6-DOF pose tracking control. Theoretical comparison and simulation results showed uniform asymptotic convergence of the controllers around the equilibrium points. However, their work considered the position and attitude separately, which led to complex control design and calculation requirements. Sun and Huo [19] proposed a robust integrated and adaptive backstepping approach that managed modeling uncertainties for spacecraft rendezvous by considering the dynamic coupling between the relative translational and rotational motion, whereas Sun et al. [20] proposed a nonlinear adaptive pose tracking control law based on the immersion and invariance approach that implemented the position and

Presented as Paper 2020-1598 at the AIAA SciTech 2020 Forum, Orlando, FL, January 6–10, 2020; received 18 February 2020; revision received 15 July 2020; accepted for publication 18 November 2021; published online 10 January 2022. Copyright © 2021 by Abin Alex Pothen, Alexander Crain, and Steve Ulrich. Published by the American Institute of Aeronautics and Astronautics, Inc., with permission. All requests for copying and permission to reprint should be submitted to CCC at www.copyright.com; employ the eISSN 1533-3884 to initiate your request. See also AIAA Rights and Permissions www.aiaa.org/randp.

*Graduate Student, Department of Mechanical and Aerospace Engineering, 1125 Colonel By Drive.

†Research Associate, Department of Mechanical and Aerospace Engineering, 1125 Colonel By Drive.

‡Associate Professor, Department of Mechanical and Aerospace Engineering, 1125 Colonel By Drive. Senior Member AIAA.

§www.esa.int/Our_Activities/Operations/Space_Debris/Active_debris_removal.

¶http://www.esa.int/Our_Activities/Space_Engineering_Technology/Clean_Space/ESA_s_e.Deorbit_debris_removal_mission_reborn_as_servicing_vehicle.

Downloaded by CARLETON UNIVERSITY on January 23, 2022 | http://arc.aiaa.org | DOI: 10.2514/1.G005169

attitude control separately. Their method, however, addressed the case of a cooperative target and chaser spacecraft. Zou and Kumar [21] applied terminal sliding mode control for finite time convergence in a distributed attitude control scheme. Wang et al. [22,23] proposed a sliding mode control strategy that addresses 6-DOF pose tracking control with finite time convergence characteristics applied to a spacecraft formation-flying problem. In their work, dual-quaternions integrate position and attitude information to describe the equations of motion, and these have the same form as rotation-only equations of motion expressed in quaternions. Filipe and Tsiotras [24] also used dual-quaternions to propose an adaptive robust pose tracking controller based on the 6-DOF model for spacecraft rendezvous and docking. Lee and Mesbahi [25] used dual-quaternion based dynamics to obtain a special type of model predictive controller that estimates the future system behavior based on current and previous information, while incorporating a field-of-view constraint to maintain a line of sight to the target. Their approach assumed a principal axis spin of the target that addressed only a simplified pose tracking problem, and the convex optimization step in the controller was deemed too computationally intensive. Dong et al. [26] used a modified artificial potential function with lower computational effort to achieve the pose tracking objective, while simultaneously addressing the approach path and the field-of-view constraints through the dual quaternions formalism. Theoretically, the local minima issue persists due to use of the potential functions, but the solutions suggest a conditional switching of control gains at a local minimum to allow the trajectory to change. Velocity-free controllers for pose tracking were applied by estimating the velocity using a dual-quaternion based filter [27,28]. More recently, fault-tolerant control [29,30] and control in the presence of parameter uncertainties [31] under similar mathematical background was presented. Owing to its parallelism with quaternion dynamics, a dual-quaternion controller can reuse the control scheme used for attitude stabilization to perform both position and orientation control. Note that the underlying control scheme, however, is still based on conventional approaches.

As an alternative, a simple control methodology that can provide the exact closed-form solution to the problem of pose tracking with a passive target object undergoing a general tumbling motion is sought in this work. Furthermore, it is desirable that the proposed methodology is capable of real-time commands that can efficiently maneuver the chaser to cancel relative motion and achieving alignment with respect to a specified point of interest on the target frame. A recent advancement in analytical dynamics known as the *Udwadia–Kalaba equation* (UKE) [32–36] is a suitable methodology to provide exact force commands to maintain a specified system constraint. By enforcing the pose tracking objective as a control constraint on the states of the chaser spacecraft, the desired control forces can be generated in real time. Pose tracking in a planar case using multiple chaser spacecraft was demonstrated by Pothen and Ulrich [37].

In this context, the original contribution of this work is to develop, based on the UKE framework, an elegant and relatively simple solution to compute a real-time control methodology that addresses the problem of 6-DOF spacecraft pose tracking in a gravity-gradient, J2-perturbed, low Earth orbit. In addition, the convergence of the control constrained UKE-based approach is proven using the Lyapunov stability theory. Finally, another contribution of this paper is the 3-DOF experimental validation campaign that demonstrates the performance and high repeatability of the proposed control methodology. Note that the design of the control law in this work relies on a perfect knowledge of the system parameters, its states, and the perfect realization of the control actions. Nevertheless, as demonstrated through experiments, the strategy achieves consistent tracking performance under practical limitations inherent to hardware implementation, such as measurement noise, delay, and nonideal realization of control actions.

The remainder of the paper is organized as follows: Sec. II describes the pose tracking problem, Sec. III presents the proposed pose tracking controller, Sec. IV discusses the stability, Sec. V presents the simulation results, Sec. VI details the experimental validation, and Sec. VII presents concluding remarks.

II. Problem Statement

This section introduces the various Cartesian coordinate frames and vectors used in the formulation and further states the position and orientation control objective.

A. Cartesian Coordinate Frames and Vectors

The origin of the Earth-centered-inertial (ECI) Cartesian coordinate frame is fixed at the center of the Earth. The x axis points toward the Vernal Equinox line, the z axis is along the Earth's spin axis, and the y axis completes the triad. Let the position vector of the center of mass of a target object be $\boldsymbol{r}_t$, so that, in the ECI frame, this is represented by

$$^{I}\boldsymbol{r}_t = X_t\boldsymbol{I}_x + Y_t\boldsymbol{I}_y + Z_t\boldsymbol{I}_z \tag{1}$$

where X_t, Y_t, and Z_t are components of the position vector along the unit vectors of ECI $\boldsymbol{I}_x$, $\boldsymbol{I}_y$, and $\boldsymbol{I}_z$, respectively.

Let body-fixed Cartesian coordinate frames be attached at the center of mass of either rigid body, as shown in black and red in Fig. 1. The position components of the target body-fixed frame origin are $\boldsymbol{r}_t^I = [\,X_t \quad Y_t \quad Z_t\,]^T$ and its orientation with respect to the inertial ECI frame is described by the quaternion components $\boldsymbol{u}_t^I = [\,u_{0,t} \quad u_{1,t} \quad u_{2,t} \quad u_{3,t}\,]^T$, where $u_{0,t}$ represents the scalar part, and $u_{1,t}$, $u_{2,t}$, and $u_{3,t}$ are vector parts of the quaternion. A point of interest on the target has a position vector component $\boldsymbol{p}_t^t = [\,p_{x,t} \quad p_{y,t} \quad p_{z,t}\,]^T$ that is fixed with respect to the target body-fixed frame. In a similar way, the origin of the chaser body-fixed Cartesian coordinate frame is located at $\boldsymbol{r}_c^I = [\,X_c \quad Y_c \quad Z_c\,]^T$ with respect to the inertial frame, and its orientation is described by the quaternion components $\boldsymbol{u}_c^I = [\,u_{0,c} \quad u_{1,c} \quad u_{2,c} \quad u_{3,c}\,]^T$. A vector $\boldsymbol{p}_c^c = [\,p_{x,c} \quad p_{y,c} \quad p_{z,c}\,]^T$ is defined as the alignment vector on the chaser frame, and may be used to maintain the alignment of the field of view of computer vision sensors toward the target. The direction cosine matrix that transforms the vector components from the target frame to the inertial frame is represented by $\boldsymbol{R}_{IT}$, whereas the transformation from the chaser to the inertial frame is given by $\boldsymbol{R}_{IC}$. These are written in terms of the quaternion components as

$$\boldsymbol{R}_{IT} = \begin{bmatrix} 2u_{0,t}^2 - 1 + 2u_{1,t}^2 & 2u_{1,t}u_{2,t} - 2u_{0,t}u_{3,t} & 2u_{1,t}u_{3,t} + 2u_{0,t}u_{2,t} \\ 2u_{1,t}u_{2,t} + 2u_{0,t}u_{3,t} & 2u_{0,t}^2 - 1 + 2u_{2,t}^2 & 2u_{2,t}u_{3,t} - 2u_{0,t}u_{1,t} \\ 2u_{1,t}u_{3,t} - 2u_{0,t}u_{2,t} & 2u_{2,t}u_{3,t} + 2u_{0,t}u_{1,t} & 2u_{0,t}^2 - 1 + 2u_{3,t}^2 \end{bmatrix} \tag{2}$$

$$\boldsymbol{R}_{IC} = \begin{bmatrix} 2u_{0,c}^2 - 1 + 2u_{1,c}^2 & 2u_{1,c}u_{2,c} - 2u_{0,c}u_{3,c} & 2u_{1,c}u_{3,c} + 2u_{0,c}u_{2,c} \\ 2u_{1,c}u_{2,c} + 2u_{0,c}u_{3,c} & 2u_{0,c}^2 - 1 + 2u_{2,c}^2 & 2u_{2,c}u_{3,c} - 2u_{0,c}u_{1,c} \\ 2u_{1,c}u_{3,c} - 2u_{0,c}u_{2,c} & 2u_{2,c}u_{3,c} + 2u_{0,c}u_{1,c} & 2u_{0,c}^2 - 1 + 2u_{3,c}^2 \end{bmatrix} \tag{3}$$

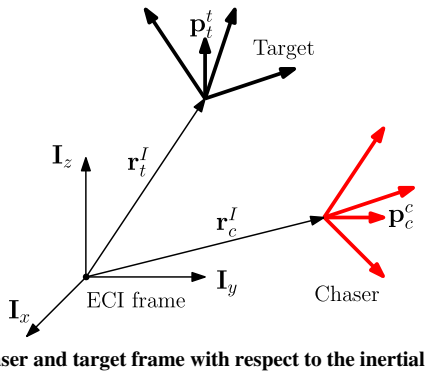

Fig. 1 Chaser and target frame with respect to the inertial ECI frame.

Downloaded by CARLETON UNIVERSITY on January 23, 2022 | http://arc.aiaa.org | DOI: 10.2514/1.G005169

B. Pose Tracking Objective

The objective of pose tracking is to simultaneously position the origin of the chaser body-fixed Cartesian coordinate frame at the specified stand-off separation L_0 with respect to the target origin, while inertially aligning $\boldsymbol{p}_c^I$ along the target point of interest vector $\boldsymbol{p}_t^I$. The unit vector along the direction of $\boldsymbol{p}_t^t$ is given by

$$\hat{\boldsymbol{p}}_t^t = \frac{\boldsymbol{p}_t^t}{\|\boldsymbol{p}_t^t\|} \tag{4}$$

Note that $\hat{\boldsymbol{p}}_t^t$ is defined with respect to the target body-fixed Cartesian coordinate frame. The required final pose of the chaser with respect to the target spacecraft is shown in Fig. 2. The control actions are used to maneuver the chaser to the final pose. Note that, in the final pose, the origin of the chaser frame is at a position $\bar{\boldsymbol{p}}_t^t$ from the target origin.

This vector is defined to be in the same direction as $\boldsymbol{p}_t^t$, with a norm corresponding to the stand-off distance L_0, that is,

$$\bar{\boldsymbol{p}}_t^t = L_0 \hat{\boldsymbol{p}}_t^t \tag{5}$$

The control acts to align the chaser position vector $\boldsymbol{r}_c^I$ at the tip of vector $\bar{\boldsymbol{p}}_t^I$, and the final position is described by

$$\boldsymbol{r}_c^I = \boldsymbol{r}_t^I + \boldsymbol{R}_{IT} \bar{\boldsymbol{p}}_t^t \tag{6}$$

The final orientation of the chaser body-fixed Cartesian coordinate frame with respect to the orientation of the target must be such that the point of interest vector $\boldsymbol{p}_t^I$ is aligned along the alignment vector $\boldsymbol{p}_c^I$, as observed from the inertial ECI frame. An alignment unit vector $\hat{\boldsymbol{p}}_c^c$ is defined in the chaser Cartesian coordinate system as

$$\hat{\boldsymbol{p}}_c^c = \frac{\boldsymbol{p}_c^c}{\|\boldsymbol{p}_c^c\|} \tag{7}$$

The orientation control objective is to inertially align $\hat{\boldsymbol{p}}_c^I$ along $\hat{\boldsymbol{p}}_t^I$, as observed from Fig. 2. In the desired final orientation, the following equation is satisfied:

$$\boldsymbol{R}_{IT} \hat{\boldsymbol{p}}_t^t = \boldsymbol{R}_{IC} \hat{\boldsymbol{p}}_c^c \tag{8}$$

where $\boldsymbol{R}_{IT}$, $\boldsymbol{R}_{IC}$, $\hat{\boldsymbol{p}}_t^t$, and $\hat{\boldsymbol{p}}_c^c$ are given by Eqs. (2–4) and (7), respectively.

III. UKE-Based Pose Tracking Control Formulation

This section focuses on developing the UKE-based control method to pose-track a specific point of interest on the target Cartesian coordinate system that is undergoing a general translating and tumbling motion.

A. Udwadia–Kalaba Equation

For completeness, this subsection reviews the Udwadia–Kalaba framework. For more details, the reader is referred to the work of Udwadia and Kalaba [32]. For a rigid body k with n generalized coordinates, the generalized unconstrained acceleration $n \times 1$ vector $\ddot{\boldsymbol{q}}_{k,u}$ is given by

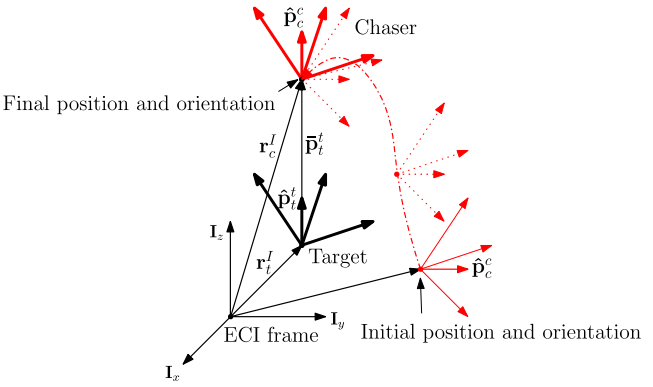

Fig. 2 Desired final pose.

$$\ddot{\boldsymbol{q}}_{k,u} = \boldsymbol{M}_{\boldsymbol{q}_k}^{-1} \boldsymbol{Q}_{\boldsymbol{q}_k} \tag{9}$$

where $\boldsymbol{M}_{\boldsymbol{q}_k}$ is the $n \times n$ generalized mass matrix and $\boldsymbol{Q}_{\boldsymbol{q}_k}$ is an $n \times 1$ vector representing the applied generalized force. Consider a set of m constraints that act on the system, which is formulated as the following matrix form:

$$\boldsymbol{A}_{\boldsymbol{q}_k} \ddot{\boldsymbol{q}}_k = \boldsymbol{b}_{\boldsymbol{q}_k} \tag{10}$$

where $\boldsymbol{A}_{\boldsymbol{q}_k}$ is an $m \times n$ matrix and $\boldsymbol{b}_{\boldsymbol{q}_k}$ is the $m \times 1$ component vector. The generalized force required to maintain the constraint is given by the Udwadia–Kalaba equation as

$$\boldsymbol{Q}_{\boldsymbol{q}_k,c} = \boldsymbol{M}_{\boldsymbol{q}_k}^{1/2} (\boldsymbol{A}_{\boldsymbol{q}_k} \boldsymbol{M}_{\boldsymbol{q}_k}^{-(1/2)})^{+} (\boldsymbol{b}_{\boldsymbol{q}_k} - \boldsymbol{A}_{\boldsymbol{q}_k} \ddot{\boldsymbol{q}}_{k,u}) \tag{11}$$

where superscript "+" denotes the Moore–Penrose pseudo-inverse. Using Eq. (11), the constrained acceleration is given by

$$\ddot{\boldsymbol{q}}_{k,c} = \ddot{\boldsymbol{q}}_{k,u} + \boldsymbol{M}_{\boldsymbol{q}_k}^{-(1/2)} (\boldsymbol{A}_{\boldsymbol{q}_k} \boldsymbol{M}_{\boldsymbol{q}_k}^{-(1/2)})^{+} (\boldsymbol{b}_{\boldsymbol{q}_k} - \boldsymbol{A}_{\boldsymbol{q}_k} \ddot{\boldsymbol{q}}_{k,u}) \tag{12}$$

B. Position Control Constraint

Using Eq. (6), the position constraint function $\boldsymbol{\Phi}_{\boldsymbol{r}}$ is defined as

$$\boldsymbol{\Phi}_{\boldsymbol{r}} = \boldsymbol{r}_t^I + \boldsymbol{R}_{IT} \bar{\boldsymbol{p}}_t^t - \boldsymbol{r}_c^I \tag{13}$$

The first derivative of Eq. (13) is given by

$$\dot{\boldsymbol{\Phi}}_{\boldsymbol{r}} = \dot{\boldsymbol{r}}_t^I + \dot{\boldsymbol{R}}_{IT} \bar{\boldsymbol{p}}_t^t + \boldsymbol{R}_{IT} \dot{\bar{\boldsymbol{p}}}_t^t - \dot{\boldsymbol{r}}_c^I \tag{14}$$

Since $\bar{\boldsymbol{p}}_t^t$ is fixed with respect to the body-fixed target frame, its time variation in this frame is $\dot{\bar{\boldsymbol{p}}}_t^t = \boldsymbol{0}$. Note that $\dot{\bar{\boldsymbol{p}}}_t^t$ is not the inertial derivative. Thus, Eq. (14) becomes

$$\dot{\boldsymbol{\Phi}}_{\boldsymbol{r}} = \dot{\boldsymbol{r}}_t^I + \dot{\boldsymbol{R}}_{IT} \bar{\boldsymbol{p}}_t^t - \dot{\boldsymbol{r}}_c^I \tag{15}$$

and taking the first derivative with respect to time, Eq. (2) yields

$$\dot{\boldsymbol{R}}_{IT} = \begin{bmatrix} 4u_{0,t}\dot{u}_{0,t} + 4u_{1,t}\dot{u}_{1,t} & \begin{matrix} 2u_{1,t}\dot{u}_{2,t} + 2u_{2,t}\dot{u}_{1,t} \\ -2u_{0,t}\dot{u}_{3,t} - 2u_{3,t}\dot{u}_{0,t} \end{matrix} & \begin{matrix} 2u_{1,t}\dot{u}_{3,t} + 2u_{3,t}\dot{u}_{1,t} \\ +2u_{0,t}\dot{u}_{2,t} + 2u_{2,t}\dot{u}_{0,t} \end{matrix} \\ \begin{matrix} 2u_{1,t}\dot{u}_{2,t} + 2u_{2,t}\dot{u}_{1,t} \\ +2u_{0,t}\dot{u}_{3,t} + 2u_{3,t}\dot{u}_{0,t} \end{matrix} & 4u_{0,t}\dot{u}_{0,t} + 4u_{2,t}\dot{u}_{2,t} & \begin{matrix} 2u_{2,t}\dot{u}_{3,t} + 2u_{3,t}\dot{u}_{2,t} \\ -2u_{0,t}\dot{u}_{1,t} - 2u_{1,t}\dot{u}_{0,t} \end{matrix} \\ \begin{matrix} 2u_{1,t}\dot{u}_{3,t} + 2u_{3,t}\dot{u}_{1,t} \\ -2u_{0,t}\dot{u}_{2,t} - 2u_{2,t}\dot{u}_{0,t} \end{matrix} & \begin{matrix} 2u_{2,t}\dot{u}_{3,t} + 2u_{3,t}\dot{u}_{2,t} \\ +2u_{0,t}\dot{u}_{1,t} + 2u_{1,t}\dot{u}_{0,t} \end{matrix} & 4u_{0,t}\dot{u}_{0,t} + 4u_{3,t}\dot{u}_{3,t} \end{bmatrix} \tag{16}$$

Downloaded by CARLETON UNIVERSITY on January 23, 2022 | http://arc.aiaa.org | DOI: 10.2514/1.G005169

Equation (16) can be expressed in an alternate form as

$$\dot{\boldsymbol{R}}_{IT} = \begin{bmatrix} \boldsymbol{L}_{1,IT}\dot{\boldsymbol{u}}_t^I & \boldsymbol{L}_{2,IT}\dot{\boldsymbol{u}}_t^I & \boldsymbol{L}_{3,IT}\dot{\boldsymbol{u}}_t^I \end{bmatrix} \tag{17}$$

where

$$\boldsymbol{L}_{1,IT} = \begin{bmatrix} 4u_{0,t} & 4u_{1,t} & 0 & 0 \\ 2u_{3,t} & 2u_{2,t} & 2u_{1,t} & 2u_{0,t} \\ -2u_{2,t} & 2u_{3,t} & -2u_{0,t} & 2u_{1,t} \end{bmatrix}$$

$$\boldsymbol{L}_{2,IT} = \begin{bmatrix} -2u_{3,t} & 2u_{2,t} & 2u_{1,t} & -2u_{0,t} \\ 4u_{0,t} & 0 & 4u_{2,t} & 0 \\ 2u_{1,t} & 2u_{0,t} & 2u_{3,t} & 2u_{2,t} \end{bmatrix}$$

$$\boldsymbol{L}_{3,IT} = \begin{bmatrix} 2u_{2,t} & 2u_{3,t} & 2u_{0,t} & 2u_{1,t} \\ -2u_{1,t} & -2u_{0,t} & 2u_{3,t} & 2u_{2,t} \\ 4u_{0,t} & 0 & 0 & 4u_{3,t} \end{bmatrix} \tag{18}$$

Substituting Eq. (17) into Eq. (15) gives

$$\dot{\boldsymbol{\Phi}}_{\boldsymbol{r}} = \dot{\boldsymbol{r}}_t^I + \bar{p}_{x,t}^t \boldsymbol{L}_{1,IT}\dot{\boldsymbol{u}}_t^I + \bar{p}_{y,t}^t \boldsymbol{L}_{2,IT}\dot{\boldsymbol{u}}_t^I + \bar{p}_{z,t}^t \boldsymbol{L}_{3,IT}\dot{\boldsymbol{u}}_t^I - \dot{\boldsymbol{r}}_c^I \tag{19}$$

The time derivative of $\dot{\boldsymbol{\Phi}}_{\boldsymbol{r}}$ results in

$$\begin{aligned} \ddot{\boldsymbol{\Phi}}_{\boldsymbol{r}} = {} & \ddot{\boldsymbol{r}}_t^I + (\bar{p}_{x,t}^t \boldsymbol{L}_{1,IT} + \bar{p}_{y,t}^t \boldsymbol{L}_{2,IT} + \bar{p}_{z,t}^t \boldsymbol{L}_{3,IT})\ddot{\boldsymbol{u}}_t^I \\ & + (\bar{p}_{x,t}^t \dot{\boldsymbol{L}}_{1,IT} + \bar{p}_{y,t}^t \dot{\boldsymbol{L}}_{2,IT} + \bar{p}_{z,t}^t \dot{\boldsymbol{L}}_{3,IT})\dot{\boldsymbol{u}}_t^I - \ddot{\boldsymbol{r}}_c^I \end{aligned} \tag{20}$$

where

$$\dot{\boldsymbol{L}}_{1,IT} = \begin{bmatrix} 4\dot{u}_{0,t} & 4\dot{u}_{1,t} & 0 & 0 \\ 2\dot{u}_{3,t} & 2\dot{u}_{2,t} & 2\dot{u}_{1,t} & 2\dot{u}_{0,t} \\ -2\dot{u}_{2,t} & 2\dot{u}_{3,t} & -2\dot{u}_{0,t} & 2\dot{u}_{1,t} \end{bmatrix}$$

$$\dot{\boldsymbol{L}}_{2,IT} = \begin{bmatrix} -2\dot{u}_{3,t} & 2\dot{u}_{2,t} & 2\dot{u}_{1,t} & -2\dot{u}_{0,t} \\ 4\dot{u}_{0,t} & 0 & 4\dot{u}_{2,t} & 0 \\ 2\dot{u}_{1,t} & 2\dot{u}_{0,t} & 2\dot{u}_{3,t} & 2\dot{u}_{2,t} \end{bmatrix}$$

$$\dot{\boldsymbol{L}}_{3,IT} = \begin{bmatrix} 2\dot{u}_{2,t} & 2\dot{u}_{3,t} & 2\dot{u}_{0,t} & 2\dot{u}_{1,t} \\ -2\dot{u}_{1,t} & -2\dot{u}_{0,t} & 2\dot{u}_{3,t} & 2\dot{u}_{2,t} \\ 4\dot{u}_{0,t} & 0 & 0 & 4\dot{u}_{3,t} \end{bmatrix} \tag{21}$$

Combining the position, velocity, and acceleration constraints, a second-order differential form is constructed as

$$\ddot{\boldsymbol{\Phi}}_{\boldsymbol{r}} + \boldsymbol{\alpha}_{\boldsymbol{r}}\dot{\boldsymbol{\Phi}}_{\boldsymbol{r}} + \boldsymbol{\gamma}_{\boldsymbol{r}}\boldsymbol{\Phi}_{\boldsymbol{r}} = \boldsymbol{0} \tag{22}$$

where $\boldsymbol{\alpha}_{\boldsymbol{r}} = \text{diag}([\alpha_x \quad \alpha_y \quad \alpha_z])$ and $\boldsymbol{\gamma}_{\boldsymbol{r}} = \text{diag}([\gamma_x \quad \gamma_y \quad \gamma_z])$ are positive definite control gain diagonal matrices that control the asymptotic convergence behavior of the desired closed loop. Using Eqs. (13), (19), and (20) in Eq. (22) results in

$$\begin{aligned} & \ddot{\boldsymbol{r}}_t^I + (\bar{p}_{x,t}^t \boldsymbol{L}_{1,IT} + \bar{p}_{y,t}^t \boldsymbol{L}_{2,IT} + \bar{p}_{z,t}^t \boldsymbol{L}_{3,IT})\ddot{\boldsymbol{u}}_t^I + (\bar{p}_{x,t}^t \dot{\boldsymbol{L}}_{1,IT} + \bar{p}_{y,t}^t \dot{\boldsymbol{L}}_{2,IT} \\ & + \bar{p}_{z,t}^t \dot{\boldsymbol{L}}_{3,IT})\dot{\boldsymbol{u}}_t^I - \ddot{\boldsymbol{r}}_c^I + \boldsymbol{\alpha}_{\boldsymbol{r}}(\dot{\boldsymbol{r}}_t^I + \bar{p}_{x,t}^t \boldsymbol{L}_{1,IT}\dot{\boldsymbol{u}}_t^I + \bar{p}_{y,t}^t \boldsymbol{L}_{2,IT}\dot{\boldsymbol{u}}_t^I \\ & + \bar{p}_{z,t}^t \boldsymbol{L}_{3,IT}\dot{\boldsymbol{u}}_t^I - \dot{\boldsymbol{r}}_c^I) + \boldsymbol{\gamma}_{\boldsymbol{r}}(\boldsymbol{r}_t^I + \boldsymbol{R}_{IT}\bar{\boldsymbol{p}}_t^t - \boldsymbol{r}_c^I) = \boldsymbol{0} \end{aligned} \tag{23}$$

After rearranging Eq. (23), $\ddot{\boldsymbol{r}}_c$ is given by

$$\begin{aligned} \ddot{\boldsymbol{r}}_c^I = {} & \ddot{\boldsymbol{r}}_t^I + (\bar{p}_{x,t}^t \boldsymbol{L}_{1,IT} + \bar{p}_{y,t}^t \boldsymbol{L}_{2,IT} + \bar{p}_{z,t}^t \boldsymbol{L}_{3,IT})\ddot{\boldsymbol{u}}_t^I + (\bar{p}_{x,t}^t \dot{\boldsymbol{L}}_{1,IT} \\ & + \bar{p}_{y,t}^t \dot{\boldsymbol{L}}_{2,IT} + \bar{p}_{z,t}^t \dot{\boldsymbol{L}}_{3,IT})\dot{\boldsymbol{u}}_t^I + \boldsymbol{\alpha}_{\boldsymbol{r}}(\dot{\boldsymbol{r}}_t^I + \bar{p}_{x,t}^t \boldsymbol{L}_{1,IT}\dot{\boldsymbol{u}}_t^I + \bar{p}_{y,t}^t \boldsymbol{L}_{2,IT}\dot{\boldsymbol{u}}_t^I \\ & + \bar{p}_{z,t}^t \boldsymbol{L}_{3,IT}\dot{\boldsymbol{u}}_t^I - \dot{\boldsymbol{r}}_c^I) + \boldsymbol{\gamma}_{\boldsymbol{r}}(\boldsymbol{r}_t^I + \boldsymbol{R}_{IT}\bar{\boldsymbol{p}}_t^t - \boldsymbol{r}_c^I) \end{aligned} \tag{24}$$

Alternatively, Eq. (24) can be written as

$$\boldsymbol{A}_{\boldsymbol{r}}\ddot{\boldsymbol{r}}_c = \boldsymbol{b}_{\boldsymbol{r}} \tag{25}$$

where $\boldsymbol{A}_{\boldsymbol{r}}$ is a 3×3 identity matrix and

$$\begin{aligned} \boldsymbol{b}_{\boldsymbol{r}} = {} & \ddot{\boldsymbol{r}}_t^I + (\bar{p}_{x,t}^t \boldsymbol{L}_{1,IT} + \bar{p}_{y,t}^t \boldsymbol{L}_{2,IT} + \bar{p}_{z,t}^t \boldsymbol{L}_{3,IT})\ddot{\boldsymbol{u}}_t^I + (\bar{p}_{x,t}^t \dot{\boldsymbol{L}}_{1,IT} \\ & + \bar{p}_{y,t}^t \dot{\boldsymbol{L}}_{2,IT} + \bar{p}_{z,t}^t \dot{\boldsymbol{L}}_{3,IT})\dot{\boldsymbol{u}}_t^I + \boldsymbol{\alpha}_{\boldsymbol{r}}(\dot{\boldsymbol{r}}_t^I + \bar{p}_{x,t}^t \boldsymbol{L}_{1,IT}\dot{\boldsymbol{u}}_t^I + \bar{p}_{y,t}^t \boldsymbol{L}_{2,IT}\dot{\boldsymbol{u}}_t^I \\ & + \bar{p}_{z,t}^t \boldsymbol{L}_{3,IT}\dot{\boldsymbol{u}}_t^I - \dot{\boldsymbol{r}}_c^I) + \boldsymbol{\gamma}_{\boldsymbol{r}}(\boldsymbol{r}_t^I + \boldsymbol{R}_{IT}\bar{\boldsymbol{p}}_t^t - \boldsymbol{r}_c^I) \end{aligned} \tag{26}$$

Equation (25) is the acceleration control constraint for the chaser stand-off distance maintenance along the target point of interest vector, as observed from the inertial frame.

C. Orientation Control Constraint

Using Eq. (8), the orientation constraint function can be written as

$$\boldsymbol{\Phi}_{\boldsymbol{u}} = \boldsymbol{R}_{IT}\hat{\boldsymbol{p}}_t^t - \boldsymbol{R}_{IC}\hat{\boldsymbol{p}}_c^c \tag{27}$$

and the first derivative of the orientation constraint of Eq. (27) with respect to time is given by

$$\dot{\boldsymbol{\Phi}}_{\boldsymbol{u}} = \dot{\boldsymbol{R}}_{IT}\hat{\boldsymbol{p}}_t^t + \boldsymbol{R}_{IT}\dot{\hat{\boldsymbol{p}}}_t^t - \dot{\boldsymbol{R}}_{IC}\hat{\boldsymbol{p}}_c^c - \boldsymbol{R}_{IC}\dot{\hat{\boldsymbol{p}}}_c^c \tag{28}$$

The unit vectors along the direction of the point of interest and alignment vectors in their respective body-fixed frames are fixed, so that $\dot{\hat{\boldsymbol{p}}}_t^t = \dot{\hat{\boldsymbol{p}}}_c^c = \boldsymbol{0}$. As before, $\hat{\boldsymbol{p}}_t^t$ and $\hat{\boldsymbol{p}}_c^c$ are not the inertial derivatives; thus Eq. (28) is reduced to

$$\dot{\boldsymbol{\Phi}}_{\boldsymbol{u}} = \dot{\boldsymbol{R}}_{IT}\hat{\boldsymbol{p}}_t^t - \dot{\boldsymbol{R}}_{IC}\hat{\boldsymbol{p}}_c^c \tag{29}$$

The rotation matrix derivative $\dot{\boldsymbol{R}}_{IT}$ is given by Eq. (17), whereas $\dot{\boldsymbol{R}}_{IC}$ is given by

$$\dot{\boldsymbol{R}}_{IC} = \begin{bmatrix} \boldsymbol{L}_{1,IC}\dot{\boldsymbol{u}}_c^I & \boldsymbol{L}_{2,IC}\dot{\boldsymbol{u}}_c^I & \boldsymbol{L}_{3,IC}\dot{\boldsymbol{u}}_c^I \end{bmatrix} \tag{30}$$

In Eq. (30), $\dot{\boldsymbol{u}}_c^I$ denotes the chaser quaternion derivative, whereas $\boldsymbol{L}_{1,IC}$, $\boldsymbol{L}_{2,IC}$, and $\boldsymbol{L}_{3,IC}$ are functions of $\boldsymbol{u}_c^I = \begin{bmatrix} u_{0,c} & u_{1,c} & u_{2,c} & u_{3,c} \end{bmatrix}^T$, and are given as

$$\boldsymbol{L}_{1,IC} = \begin{bmatrix} 4u_{0,c} & 4u_{1,c} & 0 & 0 \\ 2u_{3,c} & 2u_{2,c} & 2u_{1,c} & 2u_{0,c} \\ -2u_{2,c} & 2u_{3,c} & -2u_{0,c} & 2u_{1,c} \end{bmatrix}$$

$$\boldsymbol{L}_{2,IC} = \begin{bmatrix} -2u_{3,c} & 2u_{2,c} & 2u_{1,c} & -2u_{0,c} \\ 4u_{0,c} & 0 & 4u_{2,c} & 0 \\ 2u_{1,c} & 2u_{0,c} & 2u_{3,c} & 2u_{2,c} \end{bmatrix}$$

$$\boldsymbol{L}_{3,IC} = \begin{bmatrix} 2u_{2,c} & 2u_{3,c} & 2u_{0,c} & 2u_{1,c} \\ -2u_{1,c} & -2u_{0,c} & 2u_{3,c} & 2u_{2,c} \\ 4u_{0,c} & 0 & 0 & 4u_{3,c} \end{bmatrix} \tag{31}$$

The second derivative with respect to time of Eq. (27) is given by

$$\boldsymbol{\Phi}_{\boldsymbol{u}} = \ddot{\boldsymbol{R}}_{IT}\hat{\boldsymbol{p}}_t^t + \dot{\boldsymbol{R}}_{IT}\dot{\hat{\boldsymbol{p}}}_t^t - \ddot{\boldsymbol{R}}_{IC}\hat{\boldsymbol{p}}_c^c - \dot{\boldsymbol{R}}_{IC}\dot{\hat{\boldsymbol{p}}}_c^c \tag{32}$$

As the point of interest vector and alignment vector are fixed in their respective body frames, their derivatives become zero and Eq. (28) is simplified to

$$\boldsymbol{\Phi}_{\boldsymbol{u}} = \ddot{\boldsymbol{R}}_{IT}\hat{\boldsymbol{p}}_t^t - \ddot{\boldsymbol{R}}_{IC}\hat{\boldsymbol{p}}_c^c \tag{33}$$

The double derivative of the rotation matrix $\boldsymbol{R}_{IT}$ in Eq. (33) is given by

$$\ddot{\boldsymbol{R}}_{IT} = \begin{bmatrix} \boldsymbol{L}_{1,IT}\ddot{\boldsymbol{u}}_t^I + \dot{\boldsymbol{L}}_{1,IT}\dot{\boldsymbol{u}}_t^I & \boldsymbol{L}_{2,IT}\ddot{\boldsymbol{u}}_t^I + \dot{\boldsymbol{L}}_{2,IT}\dot{\boldsymbol{u}}_t^I & \boldsymbol{L}_{3,IT}\ddot{\boldsymbol{u}}_t^I + \dot{\boldsymbol{L}}_{3,IT}\dot{\boldsymbol{u}}_t^I \end{bmatrix} \tag{34}$$

Further, $\ddot{\boldsymbol{R}}_{IC}$ from Eq. (33) is expressed as

$$\ddot{\boldsymbol{R}}_{IC} = \begin{bmatrix} \boldsymbol{L}_{1,IC}\ddot{\boldsymbol{u}}_c^I + \dot{\boldsymbol{L}}_{1,IC}\dot{\boldsymbol{u}}_c^I & \boldsymbol{L}_{2,IC}\ddot{\boldsymbol{u}}_c^I + \dot{\boldsymbol{L}}_{2,IC}\dot{\boldsymbol{u}}_c^I & \boldsymbol{L}_{3,IC}\ddot{\boldsymbol{u}}_c^I + \dot{\boldsymbol{L}}_{3,IC}\dot{\boldsymbol{u}}_c^I \end{bmatrix} \tag{35}$$

where $\dot{\boldsymbol{L}}_{1,IC}$, $\dot{\boldsymbol{L}}_{2,IC}$, and $\dot{\boldsymbol{L}}_{3,IC}$ are given by

$$\dot{\boldsymbol{L}}_{1,IC} = \begin{bmatrix} 4\dot{u}_{0,c} & 4\dot{u}_{1,c} & 0 & 0 \\ 2\dot{u}_{3,c} & 2\dot{u}_{2,c} & 2\dot{u}_{1,c} & 2\dot{u}_{0,c} \\ -2\dot{u}_{2,c} & 2\dot{u}_{3,c} & -2\dot{u}_{0,c} & 2\dot{u}_{1,c} \end{bmatrix}$$

$$\dot{\boldsymbol{L}}_{2,IC} = \begin{bmatrix} -2\dot{u}_{3,c} & 2\dot{u}_{2,c} & 2\dot{u}_{1,c} & -2\dot{u}_{0,c} \\ 4\dot{u}_{0,c} & 0 & 4\dot{u}_{2,c} & 0 \\ 2\dot{u}_{1,c} & 2\dot{u}_{0,c} & 2\dot{u}_{3,c} & 2\dot{u}_{2,c} \end{bmatrix}$$

$$\dot{\boldsymbol{L}}_{3,IC} = \begin{bmatrix} 2\dot{u}_{2,c} & 2\dot{u}_{3,c} & 2\dot{u}_{0,c} & 2\dot{u}_{1,c} \\ -2\dot{u}_{1,c} & -2\dot{u}_{0,c} & 2\dot{u}_{3,c} & 2\dot{u}_{2,c} \\ 4\dot{u}_{0,c} & 0 & 0 & 4\dot{u}_{3,c} \end{bmatrix} \tag{36}$$

Combining Eqs. (27), (29), and (33) into a second-order differential form yields

$$\boldsymbol{\Phi}_{\boldsymbol{u}} + \boldsymbol{\alpha}_{\boldsymbol{u}}\dot{\boldsymbol{\Phi}}_{\boldsymbol{u}} + \boldsymbol{\gamma}_{\boldsymbol{u}}\boldsymbol{\Phi}_{\boldsymbol{u}} = \boldsymbol{0} \tag{37}$$

Substituting Eqs. (27), (29), and (33) into Eq. (37) gives

$$\ddot{\boldsymbol{R}}_{IT}\hat{\boldsymbol{p}}_t^t - \ddot{\boldsymbol{R}}_{IC}\hat{\boldsymbol{p}}_c^c + \boldsymbol{\alpha}_{\boldsymbol{u}}(\dot{\boldsymbol{R}}_{IT}\hat{\boldsymbol{p}}_t^t - \dot{\boldsymbol{R}}_{IC}\hat{\boldsymbol{p}}_c^c) + \boldsymbol{\gamma}_{\boldsymbol{u}}(\boldsymbol{R}_{IT}\hat{\boldsymbol{p}}_t^t - \boldsymbol{R}_{IC}\hat{\boldsymbol{p}}_c^c) = 0 \tag{38}$$

and substituting for $\ddot{\boldsymbol{R}}_{IT}$ and $\ddot{\boldsymbol{R}}_{IC}$ from Eqs. (34) and (35), respectively, into Eq. (38) yields

$$\begin{aligned} &\begin{bmatrix} \boldsymbol{L}_{1,IT}\ddot{\boldsymbol{u}}_t^I + \dot{\boldsymbol{L}}_{1,IT}\dot{\boldsymbol{u}}_t^I & \boldsymbol{L}_{2,IT}\ddot{\boldsymbol{u}}_t^I + \dot{\boldsymbol{L}}_{2,IT}\dot{\boldsymbol{u}}_t^I & \boldsymbol{L}_{3,IT}\ddot{\boldsymbol{u}}_t^I + \dot{\boldsymbol{L}}_{3,IT}\dot{\boldsymbol{u}}_t^I \end{bmatrix}\hat{\boldsymbol{p}}_t^t \\ &- \begin{bmatrix} \boldsymbol{L}_{1,IC}\ddot{\boldsymbol{u}}_c^I + \dot{\boldsymbol{L}}_{1,IC}\dot{\boldsymbol{u}}_c^I & \boldsymbol{L}_{2,IC}\ddot{\boldsymbol{u}}_c^I + \dot{\boldsymbol{L}}_{2,IC}\dot{\boldsymbol{u}}_c^I & \boldsymbol{L}_{3,IC}\ddot{\boldsymbol{u}}_c^I + \dot{\boldsymbol{L}}_{3,IC}\dot{\boldsymbol{u}}_c^I \end{bmatrix}\hat{\boldsymbol{p}}_c^c \\ &+ \boldsymbol{\alpha}_{\boldsymbol{u}}(\dot{\boldsymbol{R}}_{IT}\hat{\boldsymbol{p}}_t^t - \dot{\boldsymbol{R}}_{IC}\hat{\boldsymbol{p}}_c^c) + \boldsymbol{\gamma}_{\boldsymbol{u}}(\boldsymbol{R}_{IT}\hat{\boldsymbol{p}}_t^t - \boldsymbol{R}_{IC}\hat{\boldsymbol{p}}_c^c) = 0 \end{aligned} \tag{39}$$

Defining the body-frame components of the point of interest vector and the alignment vector as $\hat{\boldsymbol{p}}_t^t = [\,\hat{p}_{x,t}^t \quad \hat{p}_{y,t}^t \quad \hat{p}_{z,t}^t\,]^T$ and $\hat{\boldsymbol{p}}_c^c = [\,\hat{p}_{x,c}^c \quad \hat{p}_{y,c}^c \quad \hat{p}_{z,c}^c\,]^T$, respectively, and then substituting $\hat{\boldsymbol{p}}_t^t$ and $\hat{\boldsymbol{p}}_c^c$ into the first two terms of the left-hand side of Eq. (39) results in

$$\begin{aligned} &\hat{p}_{x,c}^c\boldsymbol{L}_{1,IC}\ddot{\boldsymbol{u}}_c^I + \hat{p}_{y,c}^c\boldsymbol{L}_{2,IC}\ddot{\boldsymbol{u}}_c^I + \hat{p}_{z,c}^c\boldsymbol{L}_{3,IC}\ddot{\boldsymbol{u}}_c^I + \hat{p}_{x,c}^c\dot{\boldsymbol{L}}_{1,IC}\dot{\boldsymbol{u}}_c^I \\ &\quad + \hat{p}_{y,c}^c\dot{\boldsymbol{L}}_{2,IC}\dot{\boldsymbol{u}}_c^I + \hat{p}_{z,c}^c\dot{\boldsymbol{L}}_{3,IC}\dot{\boldsymbol{u}}_c^I \\ &\quad = \hat{p}_{x,t}^t\boldsymbol{L}_{1,IT}\ddot{\boldsymbol{u}}_t^I + \hat{p}_{y,t}^t\boldsymbol{L}_{2,IT}\ddot{\boldsymbol{u}}_t^I + \hat{p}_{z,t}^t\boldsymbol{L}_{3,IT}\ddot{\boldsymbol{u}}_t^I + \hat{p}_{x,t}^t\dot{\boldsymbol{L}}_{1,IT}\dot{\boldsymbol{u}}_t^I \\ &\quad + \hat{p}_{y,t}^t\dot{\boldsymbol{L}}_{2,IT}\dot{\boldsymbol{u}}_t^I + \hat{p}_{z,t}^t\dot{\boldsymbol{L}}_{3,IT}\dot{\boldsymbol{u}}_t^I + \boldsymbol{\alpha}_{\boldsymbol{u}}(\dot{\boldsymbol{R}}_{IT}\hat{\boldsymbol{p}}_t^t - \dot{\boldsymbol{R}}_{IC}\hat{\boldsymbol{p}}_c^c) \\ &\quad + \boldsymbol{\gamma}_{\boldsymbol{u}}(\boldsymbol{R}_{IT}\hat{\boldsymbol{p}}_t^t - \boldsymbol{R}_{IC}\hat{\boldsymbol{p}}_c^c) \end{aligned} \tag{40}$$

Now, Eq. (40) is rearranged to keep the term of the chaser quaternion double derivative to the left-hand side of the equation as follows:

$$\begin{aligned} &(\hat{p}_{x,c}^c\boldsymbol{L}_{1,IC} + \hat{p}_{y,c}^c\boldsymbol{L}_{2,IC} + \hat{p}_{z,c}^c\boldsymbol{L}_{3,IC})\ddot{\boldsymbol{u}}_c^I \\ &\quad = (\hat{p}_{x,t}^t\boldsymbol{L}_{1,IT} + \hat{p}_{y,t}^t\boldsymbol{L}_{2,IT} + \hat{p}_{z,t}^t\boldsymbol{L}_{3,IT})\ddot{\boldsymbol{u}}_t^I + (\hat{p}_{x,t}^t\dot{\boldsymbol{L}}_{1,IT} + \hat{p}_{y,t}^t\dot{\boldsymbol{L}}_{2,IT} \\ &\quad + \hat{p}_{z,t}^t\dot{\boldsymbol{L}}_{3,IT})\dot{\boldsymbol{u}}_t^I - (\hat{p}_{x,c}^c\dot{\boldsymbol{L}}_{1,IC} + \hat{p}_{y,c}^c\dot{\boldsymbol{L}}_{2,IC} + \hat{p}_{z,c}^c\dot{\boldsymbol{L}}_{3,IC})\dot{\boldsymbol{u}}_c^I \\ &\quad + \boldsymbol{\alpha}_{\boldsymbol{u}}(\dot{\boldsymbol{R}}_{IT}\hat{\boldsymbol{p}}_t^t - \dot{\boldsymbol{R}}_{IC}\hat{\boldsymbol{p}}_c^c) + \boldsymbol{\gamma}_{\boldsymbol{u}}(\boldsymbol{R}_{IT}\hat{\boldsymbol{p}}_t^t - \boldsymbol{R}_{IC}\hat{\boldsymbol{p}}_c^c) \end{aligned} \tag{41}$$

Alternatively, Eq. (41) can be rewritten concisely as

$$\boldsymbol{A}_{\boldsymbol{u}}\ddot{\boldsymbol{u}}_c^I = \boldsymbol{b}_{\boldsymbol{u}} \tag{42}$$

where

$$\boldsymbol{A}_{\boldsymbol{u}} = \hat{p}_{x,c}^c\boldsymbol{L}_{1,IC} + \hat{p}_{y,c}^c\boldsymbol{L}_{2,IC} + \hat{p}_{z,c}^c\boldsymbol{L}_{3,IC} \tag{43}$$

$$\begin{aligned} \boldsymbol{b}_{\boldsymbol{u}} &= (\hat{p}_{x,t}^t\boldsymbol{L}_{1,IT} + \hat{p}_{y,t}^t\boldsymbol{L}_{2,IT} + \hat{p}_{z,t}^t\boldsymbol{L}_{3,IT})\ddot{\boldsymbol{u}}_t^I \\ &\quad + (\hat{p}_{x,t}^t\dot{\boldsymbol{L}}_{1,IT} + \hat{p}_{y,t}^t\dot{\boldsymbol{L}}_{2,IT} + \hat{p}_{z,t}^t\dot{\boldsymbol{L}}_{3,IT})\dot{\boldsymbol{u}}_t^I \\ &\quad - (\hat{p}_{x,c}^c\dot{\boldsymbol{L}}_{1,IC} + \hat{p}_{y,c}^c\dot{\boldsymbol{L}}_{2,IC} + \hat{p}_{z,c}^c\dot{\boldsymbol{L}}_{3,IC})\dot{\boldsymbol{u}}_c^I \\ &\quad + \boldsymbol{\alpha}_{\boldsymbol{u}}(\dot{\boldsymbol{R}}_{IT}\hat{\boldsymbol{p}}_t^t - \dot{\boldsymbol{R}}_{IC}\hat{\boldsymbol{p}}_c^c) + \boldsymbol{\gamma}_{\boldsymbol{u}}(\boldsymbol{R}_{IT}\hat{\boldsymbol{p}}_t^t - \boldsymbol{R}_{IC}\hat{\boldsymbol{p}}_c^c) \end{aligned} \tag{44}$$

Then Eq. (42) is the quaternion constraint equation that can be used to generate control torque that orients the chaser's alignment vector along the target point of interest vector.

D. Unconstrained Acceleration

The unconstrained acceleration is determined according to the models used for externally applied forces for the position components and the quaternion dynamics for the tumbling motion. Accounting for the dominant J_2 orbital perturbation, the net gravitational acceleration of a spacecraft k in low Earth orbit is given by

$$\ddot{\boldsymbol{r}}_k^I = -\frac{\mu}{r_k^3}\boldsymbol{r}_k^I + \boldsymbol{a}_{J_2} \tag{45}$$

where $\boldsymbol{r}_k^I = [\,X_k \quad Y_k \quad Z_k\,]^T$ denotes the Cartesian position components of either space vehicle in ECI, such that $r_k = \|\boldsymbol{r}_k^I\|$; $\mu = 398{,}600 \times 10^9$ m^3/s^2 is the standard gravitational parameter, and $\boldsymbol{a}_{J_2}$ represents the perturbing acceleration due to the oblateness of the Earth, which is mathematically described as

$$\boldsymbol{a}_{J_2} = -\frac{3}{2}J_2\frac{\mu R^2}{r_k^4}\begin{bmatrix} \left(1 - 5\left(\frac{Z_k}{r_k}\right)^2\right)\frac{X_k}{r_k} \\ \left(1 - 5\left(\frac{Z_k}{r_k}\right)^2\right)\frac{Y_k}{r_k} \\ \left(3 - 5\left(\frac{Z_k}{r_k}\right)^2\right)\frac{Z_k}{r_k} \end{bmatrix} \tag{46}$$

where $J_2 = 1.0826269 \times 10^{-3}$ is the coefficient of the second zonal harmonic of Earth's potential and $R = 6378 \times 10^3$ m is the mean equatorial radius of the Earth. As shown in Refs. [33,35], the resulting quaternion acceleration vector under the unit vector constraint is given by

$$\ddot{\boldsymbol{u}}_k^I = -\frac{1}{2}\boldsymbol{E}_{1,k}^T\tilde{\boldsymbol{J}}_k^{-1}\tilde{\boldsymbol{\omega}}_k\tilde{\boldsymbol{J}}_k\boldsymbol{\omega}_k - (\dot{\boldsymbol{u}}_k^{IT}\dot{\boldsymbol{u}}_k^I)\boldsymbol{u}_k^I \tag{47}$$

where

$$\tilde{\boldsymbol{J}}_k = \begin{bmatrix} J_{x,k} & 0 & 0 \\ 0 & J_{y,k} & 0 \\ 0 & 0 & J_{z,k} \end{bmatrix} \qquad \tilde{\boldsymbol{\omega}}_k = \begin{bmatrix} 0 & -\omega_{z,k} & \omega_{y,k} \\ \omega_{z,k} & 0 & -\omega_{x,k} \\ -\omega_{y,k} & \omega_{x,k} & 0 \end{bmatrix}$$

$$\boldsymbol{E}_{1,k} = \begin{bmatrix} -u_{1,k} & u_{0,k} & u_{3,k} & -u_{2,k} \\ -u_{2,k} & -u_{3,k} & u_{0,k} & u_{1,k} \\ -u_{3,k} & u_{2,k} & -u_{1,k} & u_{0,k} \end{bmatrix}$$

Under the effect of gravity gradient torque, the resulting tumbling motion is affected by the body-fixed torque Γ_{GG} as given by

$$\boldsymbol{\Gamma}_{GG,k}^k = \frac{3\mu}{r_k^5}\begin{bmatrix} Y_kZ_k(J_{y,k} - J_{z,k}) \\ Z_kX_k(J_{z,k} - J_{x,k}) \\ X_kY_k(J_{x,k} - J_{y,k}) \end{bmatrix} \tag{48}$$

Downloaded by CARLETON UNIVERSITY on January 23, 2022 | http://arc.aiaa.org | DOI: 10.2514/1.G005169

and the quaternion torque is obtained as

$$\boldsymbol{\Gamma}^{I}_{\boldsymbol{u,GG,k}} = 2\boldsymbol{E}^{T}_{1,k}\boldsymbol{\Gamma}^{k}_{GG,k} \tag{49}$$

Further, the generalized displacement vector of the coupled motion is defined as

$$\boldsymbol{q}_k \triangleq \begin{bmatrix} \boldsymbol{r}^{IT}_k & \boldsymbol{u}^{IT}_k \end{bmatrix}^T \tag{50}$$

and the generalized acceleration vector is given by

$$\ddot{\boldsymbol{q}}_{k,u} = \begin{bmatrix} -\frac{\mu}{r^3_k}\boldsymbol{r}^I_k + \boldsymbol{a}_{J2} \\ -\frac{1}{2}\boldsymbol{E}^T_{1,k}\boldsymbol{J}^{-1}_k\tilde{\boldsymbol{\omega}}_k\boldsymbol{J}_k\boldsymbol{\omega}_k - (\dot{\boldsymbol{u}}^{IT}_k\dot{\boldsymbol{u}}^I_k)\boldsymbol{u}^I_k + \Gamma^I_{\boldsymbol{u,GG,k}} \end{bmatrix} \tag{51}$$

This generalized acceleration vector describes the orbital and attitude dynamics of both spacecraft ($k = c$ for chaser, and $k = t$ for target) when no control input is applied. In other words, Eq. (51) is the expression for the unconstrained acceleration. Note that Eq. (51) is the dynamics model used for the control design of spacecraft in orbit.

E. Generalized Control Constraints

The position and orientation control constraints for the chaser spacecraft from Eqs. (25) and (42) can be combined into a single matrix form as

$$\begin{bmatrix} \boldsymbol{A_r} & \boldsymbol{0}_{3\times4} \\ \boldsymbol{0}_{4\times3} & \boldsymbol{A_u} \end{bmatrix}\begin{bmatrix} \ddot{\boldsymbol{r}}^I_c \\ \ddot{\boldsymbol{u}}^I_c \end{bmatrix} = \begin{bmatrix} \boldsymbol{b_r} \\ \boldsymbol{b_u} \end{bmatrix} \tag{52}$$

$$\Rightarrow \boldsymbol{A}_{\boldsymbol{q}_c}\ddot{\boldsymbol{q}}_c = \boldsymbol{b}_{\boldsymbol{q}_c} \tag{53}$$

where

$$\boldsymbol{A}_{\boldsymbol{q}_c} = \begin{bmatrix} \boldsymbol{A_r} & \boldsymbol{0}_{3\times4} \\ \boldsymbol{0}_{4\times3} & \boldsymbol{A_u} \end{bmatrix}, \qquad \ddot{\boldsymbol{q}}_c = \begin{bmatrix} \ddot{\boldsymbol{r}}^I_c \\ \ddot{\boldsymbol{u}}^I_c \end{bmatrix}, \quad \text{and } \boldsymbol{b}_{\boldsymbol{q}_c} = \begin{bmatrix} \boldsymbol{b_r} \\ \boldsymbol{b_u} \end{bmatrix}$$

The generalized mass matrix of the chaser spacecraft is given by

$$\boldsymbol{M}_{\boldsymbol{q}_c} = \begin{bmatrix} m_c\mathbb{I}_{3\times3} & \boldsymbol{0}_{3\times4} \\ \boldsymbol{0}_{4\times3} & \boldsymbol{E}^T_c\boldsymbol{J}_c\boldsymbol{E}_c \end{bmatrix} \tag{54}$$

where m_c is the mass of the chaser, $\boldsymbol{E}_c$ is the transformation matrix that relates quaternion derivatives to the body rates, and $\boldsymbol{J}_c$ is the augmented inertia matrix, as given by

$$\boldsymbol{E}_c = \begin{bmatrix} u_{0,c} & u_{1,c} & u_{2,c} & u_{3,c} \\ -u_{1,c} & u_{0,c} & u_{3,c} & -u_{2,c} \\ -u_{2,c} & -u_{3,c} & u_{0,c} & u_{1,c} \\ -u_{3,c} & u_{2,c} & -u_{1,c} & u_{0,c} \end{bmatrix}$$

$$\boldsymbol{J}_c = \begin{bmatrix} J_{0,c} & 0 & 0 & 0 \\ 0 & J_{x,c} & 0 & 0 \\ 0 & 0 & J_{y,c} & 0 \\ 0 & 0 & 0 & J_{z,c} \end{bmatrix} \tag{55}$$

where $J_{0,c}$ is an arbitrary positive scalar. When a control constraint of the form in Eq. (53) is applied to the unconstrained chaser spacecraft, the resulting generalized control constraint input $\boldsymbol{Q}_{\boldsymbol{q}_c,c}$ is given by

$$\boldsymbol{Q}_{\boldsymbol{q}_c,c} = \boldsymbol{M}^{1/2}_{\boldsymbol{q}_c}\left(\boldsymbol{A}_{\boldsymbol{q}_c}\boldsymbol{M}^{-(1/2)}_{\boldsymbol{q}_c}\right)^{+}\left(\boldsymbol{b}_{\boldsymbol{q}_c} - \boldsymbol{A}_{\boldsymbol{q}_c}\ddot{\boldsymbol{q}}_{c,u}\right) \tag{56}$$

The control input from Eq. (56) corrects for the constraint error while taking the applied external forces modeled by the unconstrained acceleration into account, as given in Sec. III.D.

IV. Stability

This section discusses the stability of the proposed UKE-based pose tracking control-constrained strategy. The position and orientation control constraints were generated by combining the position, velocity, and acceleration errors into a second-order dynamic system in Sec. III. In general, the constraint equation was of the form

$$\ddot{\boldsymbol{\Phi}}_{\boldsymbol{i}} + \boldsymbol{\alpha}_{\boldsymbol{i}}\dot{\boldsymbol{\Phi}}_{\boldsymbol{i}} + \boldsymbol{\gamma}_{\boldsymbol{i}}\boldsymbol{\Phi}_{\boldsymbol{i}} = \boldsymbol{0} \tag{57}$$

where $\boldsymbol{i} = \boldsymbol{r}, \boldsymbol{u}$. Note that $\boldsymbol{\alpha}_{\boldsymbol{i}}$ and $\boldsymbol{\gamma}_{\boldsymbol{i}}$ are diagonal matrices with positive diagonal elements.

Choose an attractor $\mathcal{A}$ as the zero-level set of a positive semidefinite Lyapunov function $V(\boldsymbol{\Phi}_{\boldsymbol{i}}, \dot{\boldsymbol{\Phi}}_{\boldsymbol{i}})$ that has the following properties:

1) $V(\boldsymbol{\Phi}_{\boldsymbol{i}}, \dot{\boldsymbol{\Phi}}_{\boldsymbol{i}}) = 0$ when $(\boldsymbol{\Phi}_{\boldsymbol{i}}, \dot{\boldsymbol{\Phi}}_{\boldsymbol{i}}) \in \mathcal{A}$.

2) $V(\boldsymbol{\Phi}_{\boldsymbol{i}}, \dot{\boldsymbol{\Phi}}_{\boldsymbol{i}})$ is unbounded.

3) $V(\boldsymbol{\Phi}_{\boldsymbol{i}}, \dot{\boldsymbol{\Phi}}_{\boldsymbol{i}})$ is continuously differentiable for all $(\boldsymbol{\Phi}_{\boldsymbol{i}}, \dot{\boldsymbol{\Phi}}_{\boldsymbol{i}})$ and has no local extrema.

4) $V(\boldsymbol{\Phi}_{\boldsymbol{i}}, \dot{\boldsymbol{\Phi}}_{\boldsymbol{i}})$ is not explicit in time.

A function $V(\boldsymbol{\Phi}_{\boldsymbol{i}}, \dot{\boldsymbol{\Phi}}_{\boldsymbol{i}})$ that satisfies these properties may be defined as

$$V(\boldsymbol{\Phi}_{\boldsymbol{i}}, \dot{\boldsymbol{\Phi}}_{\boldsymbol{i}}) = \begin{bmatrix} \boldsymbol{\Phi}^T_{\boldsymbol{i}} & \dot{\boldsymbol{\Phi}}^T_{\boldsymbol{i}} \end{bmatrix}\begin{bmatrix} \boldsymbol{\gamma}_{\boldsymbol{i}} & \epsilon\mathbb{I}_{i\times i} \\ \epsilon\mathbb{I}_{i\times i} & \mathbb{I}_{i\times i} \end{bmatrix}\begin{bmatrix} \boldsymbol{\Phi}_{\boldsymbol{i}} \\ \dot{\boldsymbol{\Phi}}_{\boldsymbol{i}} \end{bmatrix} \tag{58}$$

$$= \dot{\boldsymbol{\Phi}}^T_{\boldsymbol{i}}\dot{\boldsymbol{\Phi}}_{\boldsymbol{i}} + \boldsymbol{\Phi}^T_{\boldsymbol{i}}\boldsymbol{\gamma}_{\boldsymbol{i}}\boldsymbol{\Phi}_{\boldsymbol{i}} + 2\epsilon\dot{\boldsymbol{\Phi}}^T_{\boldsymbol{i}}\boldsymbol{\Phi}_{\boldsymbol{i}} \tag{59}$$

where ϵ is a infinitesimally small positive real number such that $V(\boldsymbol{\Phi}_{\boldsymbol{i}}, \dot{\boldsymbol{\Phi}}_{\boldsymbol{i}})$ is positive definite, and $\mathbb{I}_{i\times i}$ is an identity matrix of size given by the length of vector $\boldsymbol{\Phi}_{\boldsymbol{i}}$. Time derivative of the Lyapunov function from Eq. (59) yields

$$\dot{V}(\boldsymbol{\Phi}_{\boldsymbol{i}}, \dot{\boldsymbol{\Phi}}_{\boldsymbol{i}}) = 2(\dot{\boldsymbol{\Phi}}^T_{\boldsymbol{i}}\boldsymbol{\Phi}_{\boldsymbol{i}} + \boldsymbol{\Phi}^T_{\boldsymbol{i}}\boldsymbol{\gamma}_{\boldsymbol{i}}\dot{\boldsymbol{\Phi}}_{\boldsymbol{i}} + \epsilon\dot{\boldsymbol{\Phi}}^T_{\boldsymbol{i}}\dot{\boldsymbol{\Phi}}_{\boldsymbol{i}} + \varepsilon\boldsymbol{\Phi}^T_{\boldsymbol{i}}\boldsymbol{\Phi}_{\boldsymbol{i}}) \tag{60}$$

Substituting Eq. (57) in Eq. (60),

$$\dot{V}(\boldsymbol{\Phi}_{\boldsymbol{i}}, \dot{\boldsymbol{\Phi}}_{\boldsymbol{i}}) = 2(-\boldsymbol{\alpha}_{\boldsymbol{i}} + \epsilon\mathbb{I}_{i\times i})\epsilon\dot{\boldsymbol{\Phi}}^T_{\boldsymbol{i}}\dot{\boldsymbol{\Phi}}_{\boldsymbol{i}} + 2\epsilon(-\boldsymbol{\gamma}_{\boldsymbol{i}}\boldsymbol{\Phi}^T_{\boldsymbol{i}}\boldsymbol{\Phi}_{\boldsymbol{i}} - \boldsymbol{\alpha}_{\boldsymbol{i}}\boldsymbol{\Phi}^T_{\boldsymbol{i}}\dot{\boldsymbol{\Phi}}_{\boldsymbol{i}}) \tag{61}$$

$$= -2\begin{bmatrix} \boldsymbol{\Phi}^T_{\boldsymbol{i}} & \dot{\boldsymbol{\Phi}}^T_{\boldsymbol{i}} \end{bmatrix}\begin{bmatrix} \epsilon\boldsymbol{\gamma}_{\boldsymbol{i}} & \frac{1}{2}\epsilon\boldsymbol{\alpha}_{\boldsymbol{i}} \\ \frac{1}{2}\epsilon\boldsymbol{\alpha}_{\boldsymbol{i}} & \boldsymbol{\alpha}_{\boldsymbol{i}} - \epsilon\mathbb{I}_{i\times i} \end{bmatrix}\begin{bmatrix} \boldsymbol{\Phi}_{\boldsymbol{i}} \\ \dot{\boldsymbol{\Phi}}_{\boldsymbol{i}} \end{bmatrix} \tag{62}$$

Clearly, $\dot{V}(\boldsymbol{\Phi}_{\boldsymbol{i}}, \dot{\boldsymbol{\Phi}}_{\boldsymbol{i}})$ is negative definite for $\epsilon > 0$, and hence the second-order constraint dynamics is Lyapunov stable. Therefore, the states $(\boldsymbol{\Phi}_{\boldsymbol{i}}, \dot{\boldsymbol{\Phi}}_{\boldsymbol{i}})$ exponentially converge to the attractor $(0, 0)$. Since the Udwadia–Kalaba equation provides exact control force as given by Eq. (56) to maintain the Lyapunov-stable constraint, the resulting motion is stable. This proves the stability of control-constrained dynamics.

V. Simulation Results

Numerical simulations were conducted to evaluate the ability and performance of the developed UKE-based control method for achieving pose tracking in close proximity. This section presents the results obtained for a total of five cases wherein the chaser attempts rendezvous within close proximity to the target. All simulations are performed with respect to the ECI frame for both spacecraft motion, and the effect of gravity gradient torques and oblateness that causes the J_2 perturbing acceleration on the orbital motion are considered. In other words, Eq. (51) presented earlier was used to numerically propagate the orbital and attitude motion. The target is initially assumed to have position of $\boldsymbol{r}^I_{0,t} = \begin{bmatrix} 6.22712 & 3.24098 & 1.21845 \end{bmatrix}^T \times 10^6$ m and a velocity of $\boldsymbol{v}^I_{0,t} = \begin{bmatrix} -3.66458 & 5.68722 & 3.60103 \end{bmatrix}^T \times 10^3$ m/s. Target is also initially oriented along the ECI Cartesian coordinate frame with an angular rate of 0.01 rad/s along the body-fixed z axis. Consequently, the quaternion vector is given by $\boldsymbol{u}^I_{0,t} = \begin{bmatrix} 1 & 0 & 0 & 0 \end{bmatrix}^T$ and a quaternion rate of $\dot{\boldsymbol{u}}^I_{0,t} = \begin{bmatrix} 0 & 0 & 0 & 0.005 \end{bmatrix}^T$. The relative orientation of the chaser with respect to the target is obtained by offsetting the chaser

Downloaded by CARLETON UNIVERSITY on January 23, 2022 | http://arc.aiaa.org | DOI: 10.2514/1.G005169

frame along the z axis of the body-fixed Cartesian frame. The initial positions of the chaser, along with the orientation for all five cases, are tabulated in Table 1.

For all the cases, the chaser has an initial velocity of $\boldsymbol{v}^I_{0,c} = \begin{bmatrix} -3.6648 & 5.68703 & 3.60109 \end{bmatrix}^T \times 10^3$ m/s, and the quaternion rate is $\dot{\boldsymbol{u}}^I_{0,c} = \begin{bmatrix} 0 & 0 & 0 & 0 \end{bmatrix}^T$. The spacecraft is assumed to have a mass of $m_c = 50$ kg, and the principal moment of inertia $\boldsymbol{J}_c$ for the chaser is considered as

$$\boldsymbol{J}_c = \begin{bmatrix} 1.3626 & 0 & 0 \\ 0 & 1.5333 & 0 \\ 0 & 0 & 0.3848 \end{bmatrix} \tag{63}$$

The target point of interest vector is chosen as $\bar{\boldsymbol{p}}^t_t = \begin{bmatrix} 1 & 0 & 0 \end{bmatrix}^T$ m and the chaser alignment vector is given by $\hat{\boldsymbol{p}}^c_c = \begin{bmatrix} 1 & 0 & 0 \end{bmatrix}^T$ m. Chaser control gains are chosen so as to obtain a

Table 1 Initial conditions for various cases

Case	Chaser position	Chaser orientation
1: 5 km, $(5\pi/10)$ rad offset	$\boldsymbol{r}^I_{0,c} = \begin{bmatrix} 6.2315 & 3.2433 & 1.2193 \end{bmatrix}^T \times 10^6$ m	$\boldsymbol{u}^I_{0,c} = \begin{bmatrix} 0.7934 & 0 & 0 & 0.6088 \end{bmatrix}^T$
2: 1 km, $\pi/4$ rad offset	$\boldsymbol{r}^I_{0,t} = \begin{bmatrix} 6.2280 & 3.2414 & 1.2186 \end{bmatrix}^T \times 10^6$ m	$\boldsymbol{u}^I_{0,c} = \begin{bmatrix} 0.9239 & 0 & 0 & 0.3827 \end{bmatrix}^T$
3: 100 m, $\pi/6$ rad offset	$\boldsymbol{r}^I_{0,t} = \begin{bmatrix} 6.2272 & 3.2410 & 1.2185 \end{bmatrix}^T \times 10^6$ m	$\boldsymbol{u}^I_{0,c} = \begin{bmatrix} 0.9659 & 0 & 0 & 0.2588 \end{bmatrix}^T$
4: 50 m, $\pi/12$ rad offset	$\boldsymbol{r}^I_{0,t} = \begin{bmatrix} 6.2272 & 3.2410 & 1.2185 \end{bmatrix}^T \times 10^6$ m	$\boldsymbol{u}^I_{0,c} = \begin{bmatrix} 0.9914 & 0 & 0 & 0.1305 \end{bmatrix}^T$
5: 10 m, $\pi/36$ rad offset	$\boldsymbol{r}^I_{0,t} = \begin{bmatrix} 6.2271 & 3.2410 & 1.2185 \end{bmatrix}^T \times 10^6$ m	$\boldsymbol{u}^I_{0,c} = \begin{bmatrix} 0.9990 & 0 & 0 & 0.0436 \end{bmatrix}^T$

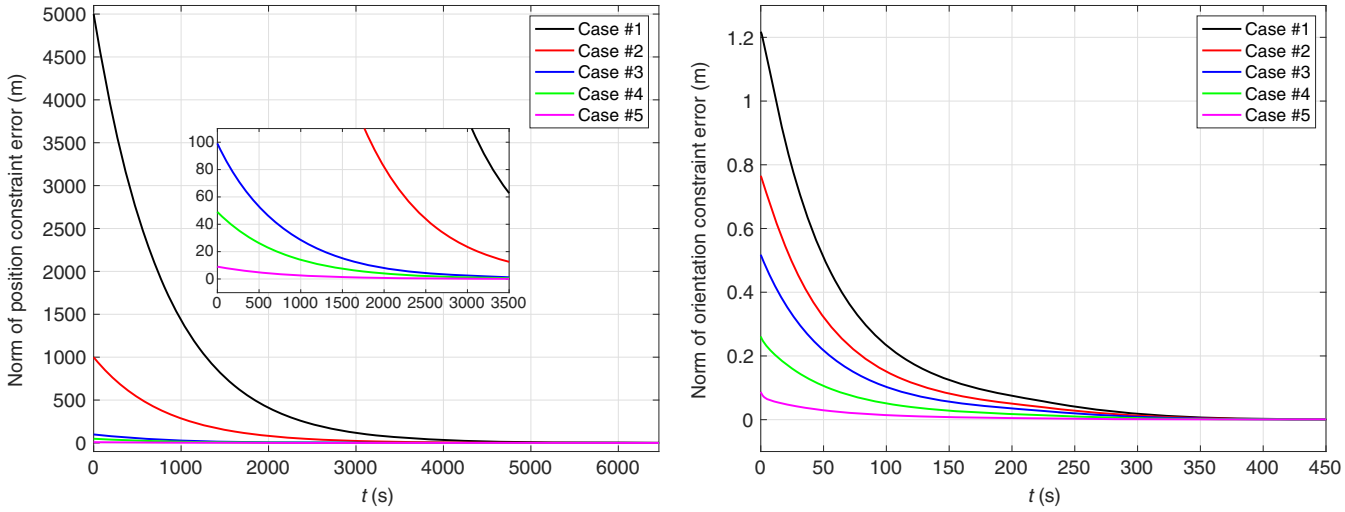

a) Position constraint error norm **b) Orientation constraint error norm**

Fig. 3 Simulation results.

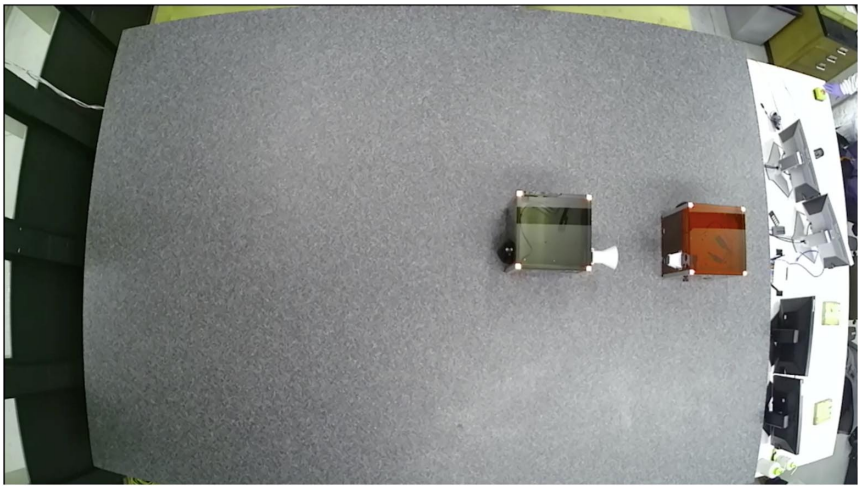

Fig. 4 Top view of SPOT with the spacecraft platforms.

Downloaded by CARLETON UNIVERSITY on January 23, 2022 | http://arc.aiaa.org | DOI: 10.2514/1.G005169

Fig. 5 The black target and red chaser spacecraft platforms.

zero error undershoot for both the position and orientation constraint error norms. The large derivative gains also introduce overdamping so that the spacecraft do not collide with each other. Meanwhile, the lower proportional gain reduces the thrust requirements. The following gains are chosen by trial and error:

$$\boldsymbol{\alpha_r} = 2 \cdot \mathbb{I}_{3\times3} \qquad \boldsymbol{\gamma_r} = 0.0025 \cdot \mathbb{I}_{3\times3} \qquad \boldsymbol{\alpha_u} = 2 \cdot \mathbb{I}_{3\times3}$$
$$\boldsymbol{\gamma_u} = 0.035 \cdot \mathbb{I}_{3\times3} \tag{64}$$

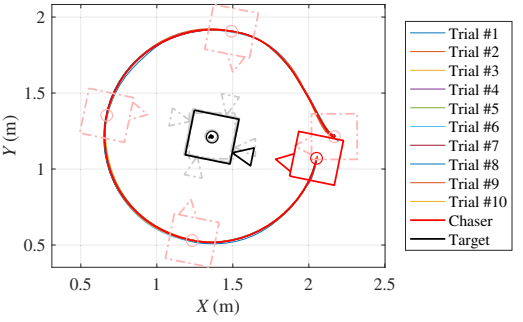

a) Chaser and target platform trajectory

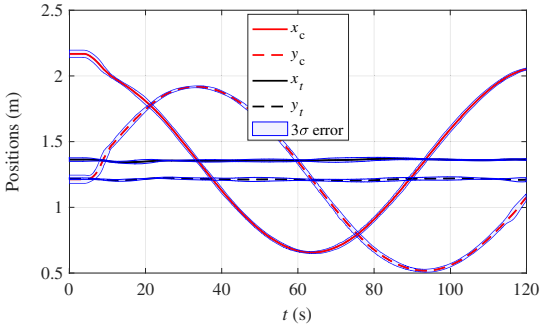

b) Position time history

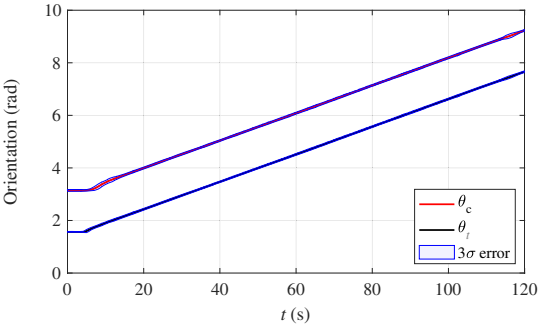

c) Orientation time history

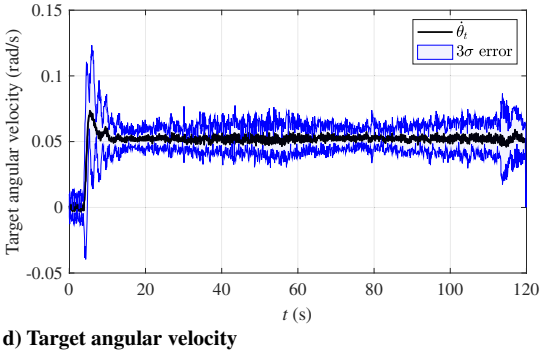

d) Target angular velocity

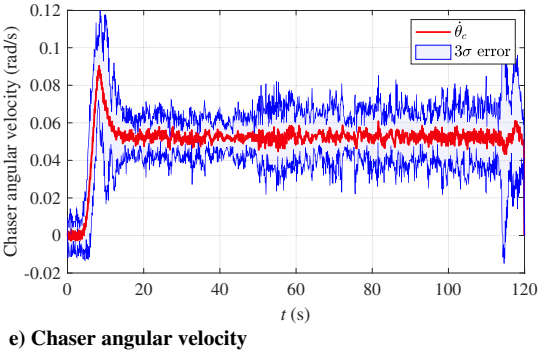

e) Chaser angular velocity

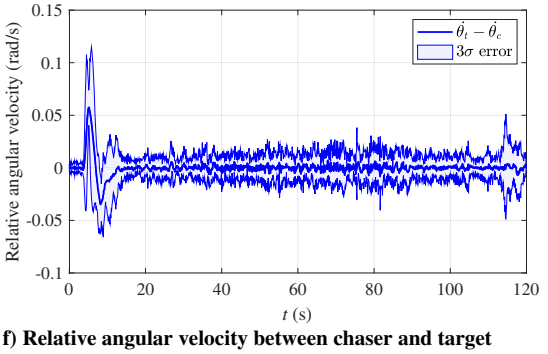

f) Relative angular velocity between chaser and target

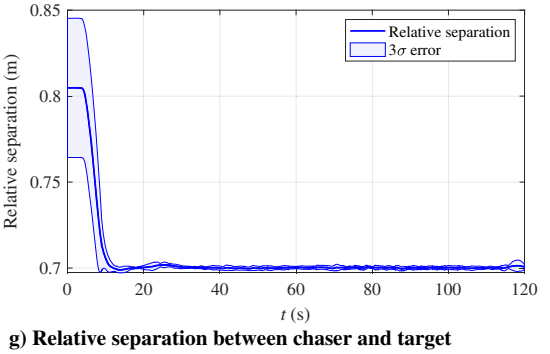

g) Relative separation between chaser and target

Fig. 6 Experimental results of pose tracking around a spinning target.

Downloaded by CARLETON UNIVERSITY on January 23, 2022 | http://arc.aiaa.org | DOI: 10.2514/1.G005169

The simulation runs for one orbital period using a fixed-step Runge–Kutta solver with a time step of 0.1 s in MATLAB/Simulink. Figure 3a shows the settling characteristics for the orientation constraint error norm, whereas the asymptotic convergence of the position constraint error norm is shown in Fig. 3b. For all five cases, the position error norms shown in Fig. 3a exhibit an overdamped response with a settling time that varies based on the initial condition. For example, case 1, which starts with the chaser spacecraft 5 km away from the target, exhibits a longer convergence time than all other cases that were initialized in closer proximity. Specifically, in case 1, the chaser spacecraft converges within 2 m of the target in 6255.7 s, compared with 4968.3, 3120.1, 2557.8, and 1203.2 s for cases 2, 3, 4, and 5, respectively. Similarly, the time history of orientation vector error norm signals provided in Fig. 3b also shows an overdamped response convergence times within 0.01 m of 332.3, 311.9, 292.8, 252.5, and 129.4 s for cases 1–5, respectively. Note that selecting different gains would result in different convergence times for both the position and orientation error signals.

VI. Planar Experimental Validation

This section presents the experimental validation of the Udwadia–Kalaba-based pose tracking controller that performs simultaneous positioning and angular orientation tracking with respect to a target spacecraft. The validation was conducted using the Spacecraft Proximity Operations Testbed (SPOT) at Carleton University's Spacecraft Robotics and Control Laboratory. The SPOT, as shown in Fig. 4, is a 3-DOF planar gravity offset test facility used to experimentally evaluate guidance, navigation, and control algorithms for spacecraft close-proximity operations.

It consists of a 3.51155 m × 2.41935 m smooth and flat granite surface on which a chaser and target platforms float on three air bearings, thereby providing an almost friction-free surface that approximates the space environment. Each platform has a dimension of 30 cm × 30 cm × 30 cm and is equipped with a 4500 psi compressed air tank. Eight air thruster nozzles are evenly distributed on the four sides, and each thruster generates a maximum thrust of 1 N. Normally closed solenoid values are used to control the opening time of each nozzle to generate the desired control force and torque demands. A simple control mixing strategy based on the least square estimate of the thrust distribution matrix among all eight air nozzles is employed [38]. In the context of this work, Eq. (56) is used for generating the control input signals, which is written using MATLAB/Simulink 2017b. The experiment is simulated before implementation on the actual platforms, and when a satisfactory simulation performance is achieved, the control blocks are transmitted to the platforms' Raspberry Pi 3 onboard computers. After the platforms are placed on the table and the experiment is initiated, the C/C++ compiled code performs the experiment automatically. During an experiment, both platforms are tracked by a PhaseSpace motion capture system that senses the spacecraft position with an accuracy of 0.1 mm. This system tracks light-emitting diodes installed on both platforms and transmit real-time state information of both platforms to the ground station computer. The computer then transmits this ground-truth dynamic state information wirelessly to both Raspberry Pi 3, and based on the received information, the flight computer generates the desired nozzle firing commands. The experiment was performed at 20 Hz, whereas data were collected at 10 Hz. This was to ensure that the data buffer does not fill up, causing the system to behave in a sub-real-time manner. Once the experiment is completed, the experimental data are recovered and stored as a *.mat* file, which can be used to plot the data. The red platform represents the chaser spacecraft, whereas the target spacecraft is the black platform as shown in Fig. 5. The red chaser is the heavier of the two platforms with a mass of 16.9478 kg and an out-of-plane inertial of 0.2709 kg · m^2. The black target platform has a mass of

Downloaded by CARLETON UNIVERSITY on January 23, 2022 | http://arc.aiaa.org | DOI: 10.2514/1.G005169

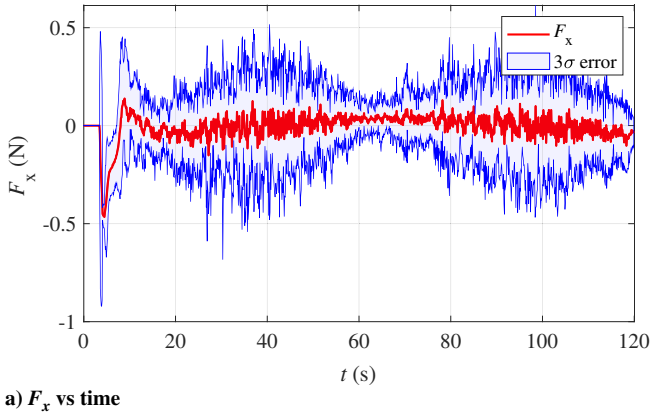

a) F_x vs time

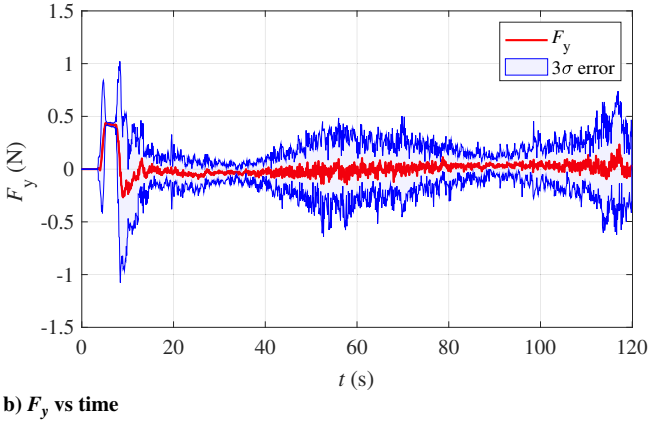

b) F_y vs time

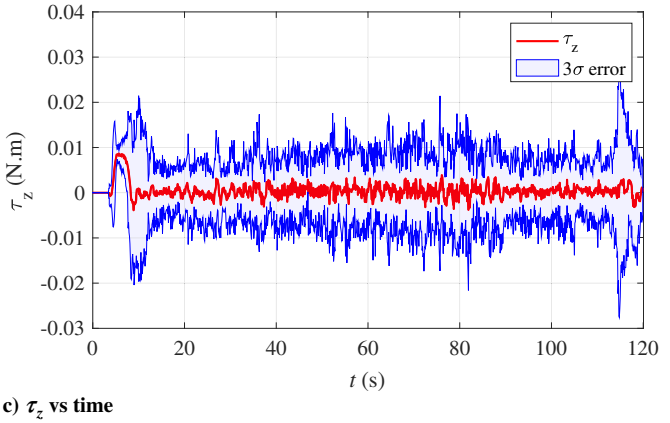

c) τ_z vs time

Fig. 7 Chaser control forces and torque for pose tracking around a spinning target.

12.3341 kg · m^2 and an out-of-plane inertia of 0.1880 kg · m^2. Note that as air is expelled through the nozzles, the mass of both the chaser and target decreases; as a result, their inertias also decrease. This variation, however, does not affect the pose tracking performance as the positive definitiveness of the generalized mass matrix is maintained.

To ensure the repeatability, a total of 30 experiments are conducted, with 10 experiment trials for each scenario. The mean of the trials is shown in the figures present in the following subsection, along with error bars calculated using the standard error. Note that the error bars represent the 99.7% (i.e., 3σ) confidence interval for the trials in each of the scenario plots.

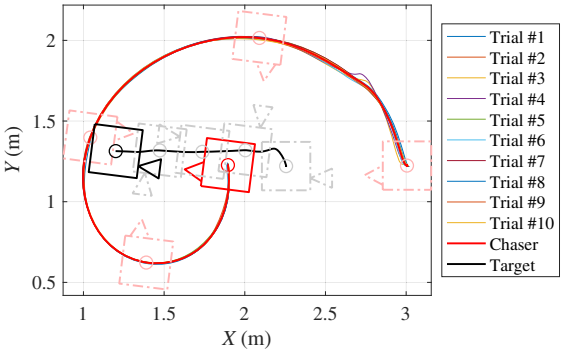

a) Chaser and target platform trajectory

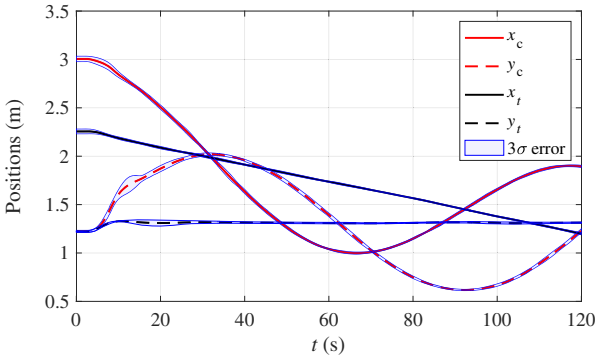

b) Position time history

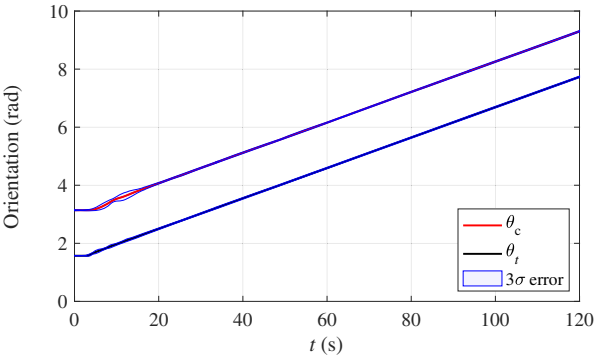

c) Orientation time history

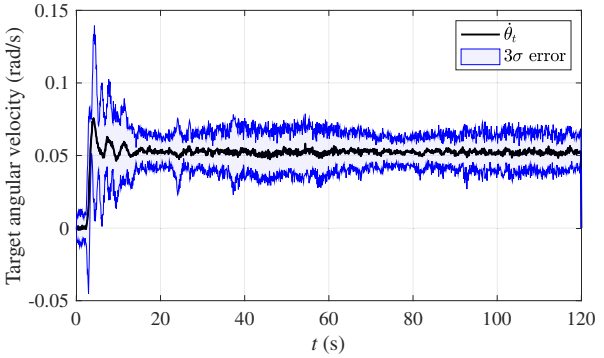

d) Target angular velocity

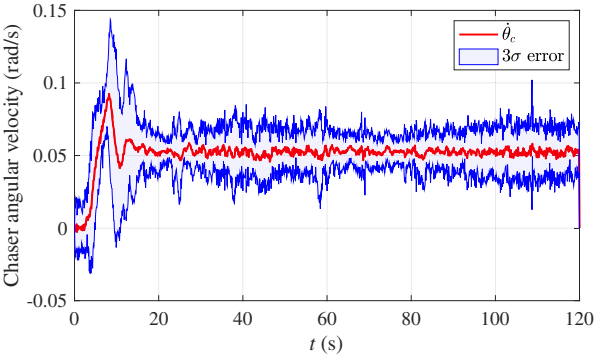

e) Chaser angular velocity

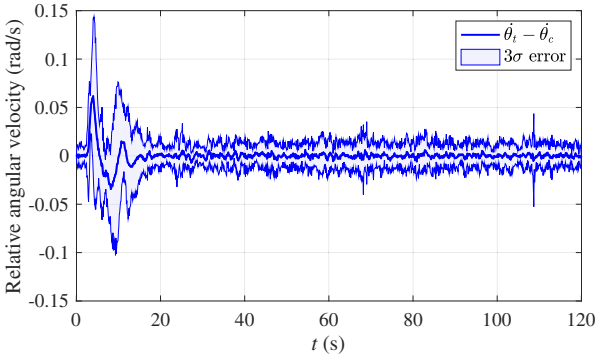

f) Relative angular velocity between chaser and target

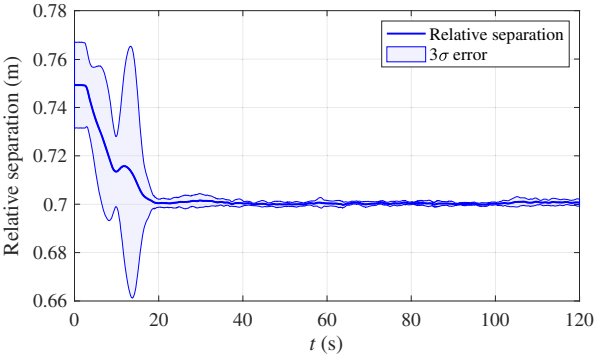

g) Relative separation between chaser and target

Fig. 8 Experimental results of pose tracking around a translating and spinning target.

Downloaded by CARLETON UNIVERSITY on January 23, 2022 | http://arc.aiaa.org | DOI: 10.2514/1.G005169

Downloaded by CARLETON UNIVERSITY on January 23, 2022 | http://arc.aiaa.org | DOI: 10.2514/1.G005169

A. Case 1: Pose Tracking Around a Spinning Target

Figure 6a illustrates the trajectories of the chaser and target platforms. Before the experiment, maneuvers are performed to maintain the chaser at (2.15578, 1.20968) m along the x and y axis, respectively, of the granite table inertial frame while, similarly, the target frame was initially positioned at (1.35577, 1.20968) m. The orientation of the chaser frame with respect to the positive x axis of the inertial frame was maintained at π rad, whereas that of the target remained at 0 rad. The experiment then ran for 120 s, during which the chaser was required to maintain the specified stand-off distance of 0.7 m with respect to the target, as shown in Fig. 6a. The corresponding variations in the x and y components are plotted in Fig. 6b. The x component of the chaser traces cosine curve around the actual x position of the target, whereas the y component follows a sine curve around the target y location, thereby resulting in a circular motion of the chaser around the target. The variation of the angular orientation of the chaser and target is plotted in Fig. 6c. The target starts at an orientation of 0 rad and continues the rotational motion until it reaches 2π rad and completes one full rotation. The chaser follows this orientation with an angular phase shift of π rad to always maintain its docking mechanism facing the target. Specifically, starting at an angular orientation of π rad, the chaser rotates until it reaches 3π rad. The time history of the angular velocity is shown in Figs. 6d and 6e. Because both platforms start from rest, their respective initial angular velocity is 0 rad/s, and then the target was commanded to rotate at a constant angular velocity of 0.0523599 rad/s as observed in Fig. 6d. Note that the chaser has no information about this commanded input of the target; it simply applies the control inputs that are calculated based on the current dynamic states and aligns its angular velocity with that of the target as shown in Fig. 6e. Figure 6f presents a plot of the relative angular velocity of the chaser with respect to the target, which diminishes to 0 with time. Desired stand-off distance between the chaser and target is 0.7 m, and the maintenance of this relative separation is observed in Fig. 6g. Finally, the chaser control input forces as a function of time are provided in Fig. 7. These commands are calculated from the chaser and target state information by applying Eq. (56). The corresponding control action ensures that stand-off distance maintenance and orientation control is simultaneously achieved to complete a pose tracking maneuver around a spinning target.

B. Case 2: Pose Tracking Around a Translating and Spinning Target

In the pose tracking experiment with a translating and spinning target object, both platforms began near one of the shorter edges of granite surface, and translating motion was established for the target along the length of table. At the beginning, the chaser was commanded to the x-y initial location of (3.05578, 1.20968) m, and the target was directed to the x-y location of (2.25577, 1.20968) m. The initial orientations of both body frames with respect to the inertial reference are the same as in case 1, and the time history of the trajectory of chaser and target platforms can be seen in Fig. 8a. As indicated, the chaser controlled its positioning to maintain the stand-off separation with respect to the translating and spinning target. Cartesian components of the position of both platforms as a function of time are shown in Fig. 8b. The chaser x position is shown to vary in a periodic manner while centered around the target x position, which is linearly decreasing. The y position of the target follows is a straight line parallel to the horizontal axis, and the corresponding chaser component approximates a sine curve centered at the target y position. Figure 8c presents the variation of spacecraft orientation, whereas the angular velocities for both the target and the chaser are presented in Figs. 8d and 8e, respectively. Note that the time-varying relative angular velocity between the chaser and target settles to 0 as shown in Fig. 8f, and the stand-off separation settles to 0.7 m as observed from Fig. 8g. The corresponding control forces and torque that simultaneously maintains the stand-off separation and orientation are shown in Fig. 9.

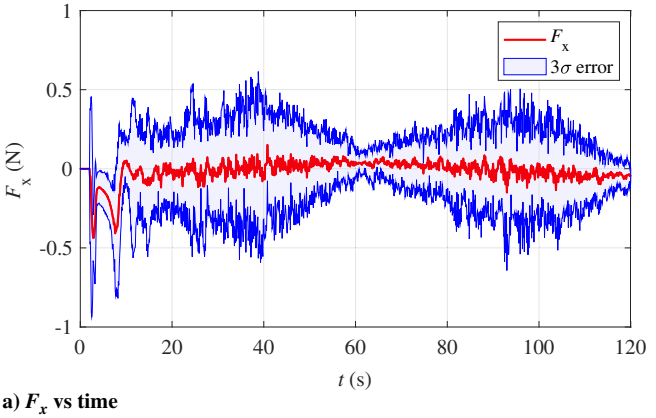

a) F_x vs time

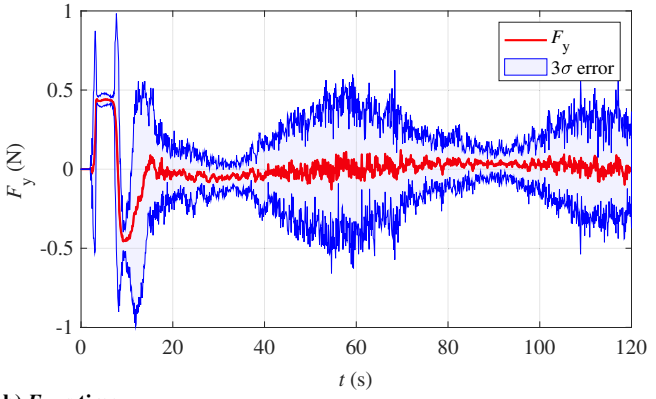

b) F_y vs time

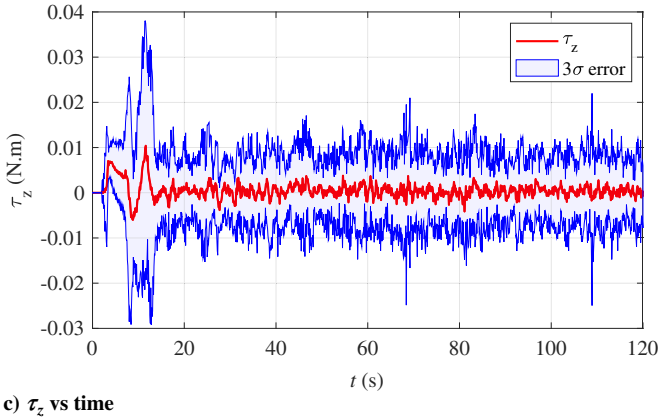

c) τ_z vs time

Fig. 9 Chaser control forces and torque for pose tracking around a translating and spinning target.

C. Case 3: Docking to a Translating and Spinning Target

In the case where the chaser alignment with respect to the target is the exact alignment of their docking ports, the proposed control method can be adapted to perform a docking maneuver. The idea is to apply the Udwadia–Kalaba-equation-based planar pose tracking method to gradually reduce L_0 to the final, required, docking separation. An important practical consideration is that L_0 reduction be initiated in the final approach along the prescribed docking mechanism's approach cone. Further, it is advantageous to decrease L_0 slowly to the desired standoff distance rather than suddenly, in order to prevent undesirable overshoots that could cause the chaser to collide with the target and push it away before the docking occurs, or in some cases, even damage the docking port.

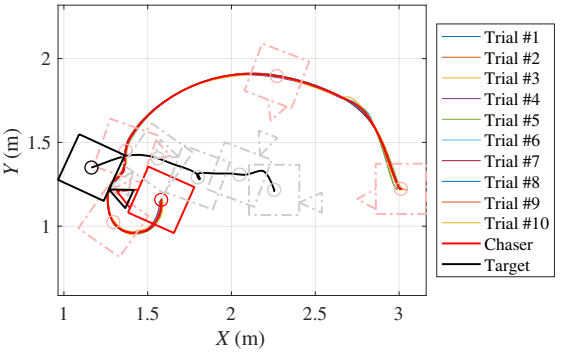

a) Chaser and target platform trajectory

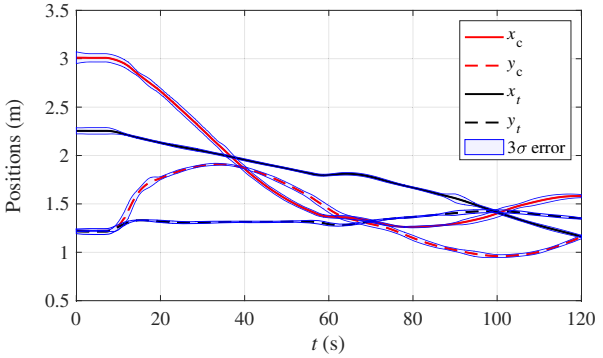

b) Position time history

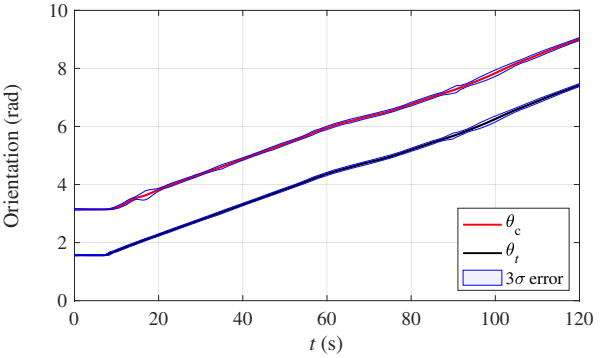

c) Orientation time history

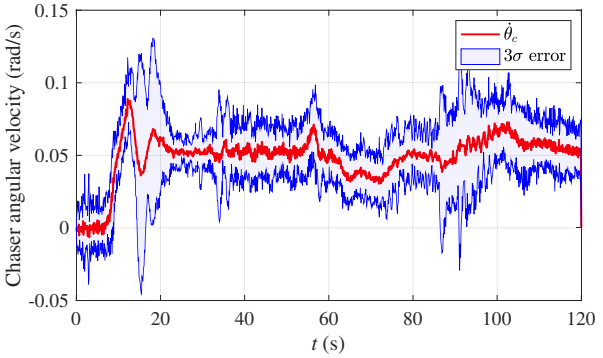

d) Target angular velocity

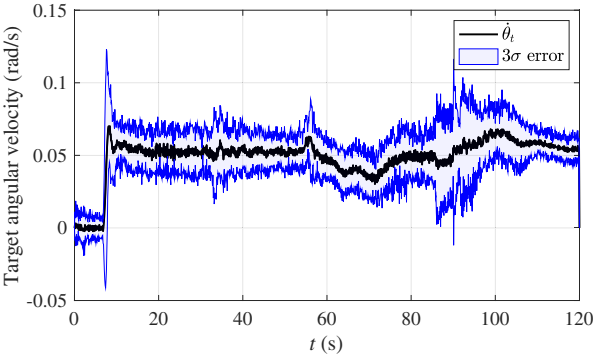

e) Chaser angular velocity

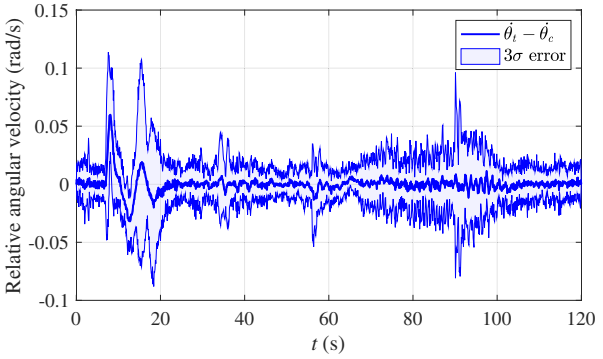

f) Relative angular velocity between chaser and target

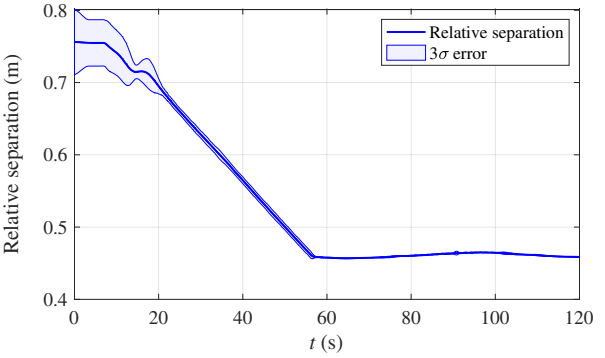

g) Relative separation between chaser and target

Fig. 10 Experimental results of docking to a translating and spinning target.

Downloaded by CARLETON UNIVERSITY on January 23, 2022 | http://arc.aiaa.org | DOI: 10.2514/1.G005169

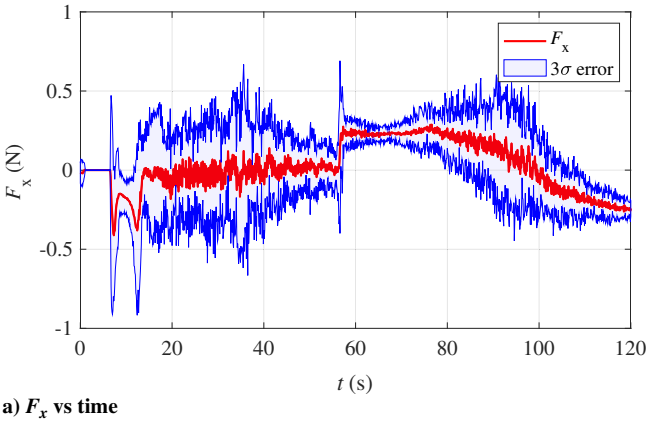

a) F_x vs time

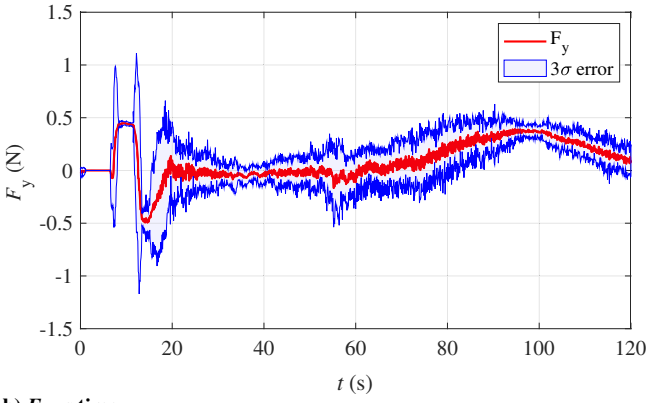

b) F_y vs time

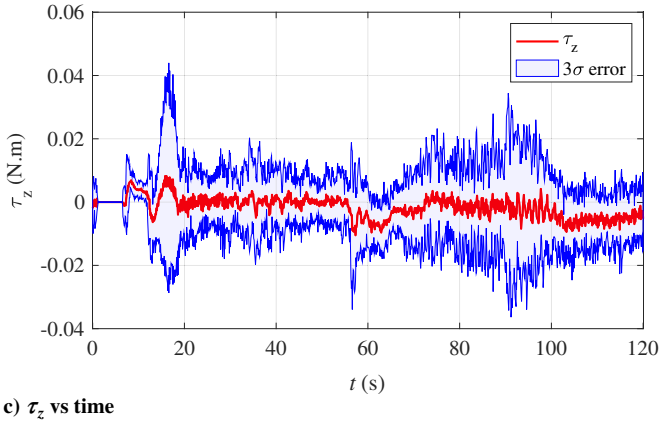

c) τ_z vs time

Fig. 11 Chaser control forces and torque for docking to a translating and spinning target.

The trajectories of the chaser and target are shown in Fig. 10a. The initial position and orientation of both the chaser and the target are the same as in case 2, as discussed in Sec. VI.B. Unlike the previous cases, a docking command was issued at 15 s.

The standoff separation was reduced from 0.7 m to the docking distance of 0.45 m as a linear function of time over a period of 40 s. Components of the position vector of the target and chaser vary as shown in Fig. 10c. Starting at a y position of 1.20968 m, the target was commanded to move to 1.30968 m, with a constant velocity along the negative x axis. The chaser platform followed the target motion based on the state information, thus performing the required pose tracking maneuver. The corresponding orientation changes are shown in Fig. 10c. Starting from an initial alignment of π rad, the chaser almost finishes a complete circle, when the experiment was completed. The target and chaser angular velocities are plotted in Figs. 10d and 10e, respectively whereas the relative angular velocity settles to 0 as observed from Fig. 10f. Figure 10g presents the variations of the standoff distance with respect to time. The docking maneuver is observed from 15 to 55 s where the distance decreases from 0.7 to 0.45 m. Finally, Fig. 11 presents the control inputs applied to accomplish the pose tracking and docking maneuvers. Note that the angular velocities and the control forces tend to destabilize immediately after the docking ports meet at 55 s into the experiment, because the body configuration changes after docking, whereas the pose tracking controller continues to act. Indeed, the proposed control law does not account for the interaction between the two rigid spacecraft in the post-docking phase.

VII. Conclusions

This paper presented the development of a spatial standoff pose tracking controller using the Udwadia–Kalaba framework. The asymptotic convergence of the position and orientation tracking errors was proven. The key advantage of this method was demonstrated in pose tracking simulations for a tumbling target in a gravity-gradient, J_2-perturbed, elliptical low Earth orbit. The controller ensured that the specified standoff distance at the required orientation is achieved, starting at several initial relative positions and orientations of the chaser spacecraft with respect to the target in close-proximity simulations. Finally, experimental validation of the Udwadia–Kalaba-equation-based standoff pose tracking controller was performed using Spacecraft Proximity Operations Testbed at Carleton University. In addition to demonstrating planar pose tracking in the case of a spinning and translating target, a docking maneuver was also presented. The experiment confirmed the viability of the developed approach to maintain standoff distance while pointing toward a location of interest on an uncontrolled target.

Acknowledgment

This work was supported in part by the Natural Sciences and Engineering Research Council of Canada under the Discovery Grant program.

References

[1] Lin, Z., Zeman, V., and Patel, R. V., "On-Line Robot Trajectory Planning for Catching a Moving Object," *IEEE International Conference on Robotics and Automation*, IEEE Publ., Piscataway, NJ, 1989, pp. 1726–1731. https://doi.org/10.1109/ROBOT.1989.100224

[2] Sharma, R., Herve, J.-Y., and Cucka, P., "Dynamic Robot Manipulation Using Visual Tracking," *IEEE International Conference on Robotics and Automation*, IEEE Publ., Piscataway, NJ, 1992, pp. 1844–1849. https://doi.org/10.1109/ROBOT.1992.219959

[3] Lei, M., and Ghosh, B. K., "Visually Guided Robotic Tracking and Grasping of a Moving Object," *IEEE Conference on Decision and Control*, IEEE Publ., Piscataway, NJ, 1993, pp. 1604–1609. https://doi.org/10.1109/CDC.1993.325458

[4] Chen, Y., and Watson, L. T., "Optimal Trajectory Planning for a Space Robot Docking with a Moving Target via Homotopy Algorithms,"

Downloaded by CARLETON UNIVERSITY on January 23, 2022 | http://arc.aiaa.org | DOI: 10.2514/1.G005169

Journal of Robotic Systems, Vol. 12, No. 8, 1995, pp. 531–540.
https://doi.org/10.1002/rob.4620120803

[5] Zhang, M., and Buehler, M., "Sensor-Based Online Trajectory Generation for Smoothly Grasping Moving Objects," *IEEE International Symposium on Intelligent Control*, IEEE Publ., Piscataway, NJ, 1994, pp. 141–146.
https://doi.org/10.1109/ISIC.1994.367827

[6] Fitz-Coy, N., and Liu, M. C., "New Modified Proportional Navigation Scheme for Rendezvous and Docking with Tumbling Targets: The Planar Case," *Symposium on Flight Mechanics/Estimation Theory*, NASA, 1995, pp. 243–252.

[7] Croft, E. A., Fenton, R. G., and Benhabib, B., "Optimal Rendezvous-Point Selection for Robotic Inteception of Moving Objects," *IEEE Transaction on Systems, Man, and Cybernetics*, Vol. 28, No. 2, 1998, pp. 192–204.
https://doi.org/10.1109/3477.662759

[8] Mehrandezh, M., Sela, N. M., Fenton, R. G., and Benhabib, B., "Robotic Interception of Moving Objects Using an Augmented Ideal Proportional Navigation Guidance Technique," *IEEE Transactions on Systems, Man, and Cybernetics*, Vol. 30, No. 3, 2000, pp. 238–250.
https://doi.org/10.1109/3468.844351

[9] Fehse, W., *Automated Rendezvous and Docking of Spacecraft*, Cambridge Univ. Press, New York, 2003, pp. 195–198.
https://doi.org/10.1109/3468.844351

[10] Ma, Z., Ma, O., and Shashikanth, B. N., "Optimal Approach to and Alignment with a Rotating Rigid Body for Capture," *Journal of the Astronautical Sciences*, Vol. 55, No. 4, 2007, pp. 407–419.
https://doi.org/10.1007/BF03256532

[11] Romano, M., Friedman, D. A., and Shay, T. J., "Laboratory Experimentation of Autonomous Spacecraft Approach and Docking to a Collaborative Target," *Journal of Spacecraft and Rockets*, Vol. 44, No. 1, 2007, pp. 164–173.
https://doi.org/10.2514/1.22092

[12] Zhang, D., Song, S., and Pei, R., "Safe Guidance for Autonomous Rendezvous and Docking with a Non-Cooperative Target," *AIAA Guidance, Navigation, and Control Conference*, AIAA Paper 2010-7592, 2010.
https://doi.org/10.2514/6.2010-7592

[13] Aghili, F., "A Prediction and Motion-Planning Scheme for Visually Guided Robotic Capturing of Free-Floating Tumbling Objects with Uncertain Dynamics," *IEEE Transactions on Robotics*, Vol. 28, No. 3, 2012, pp. 634–649.
https://doi.org/10.1109/TRO.2011.2179581

[14] Wilde, M., Ciarcià, M., Grompone, A., and Romano, M., "Experimental Characterization of Inverse Dynamics Guidance in Docking with a Rotating Target," *Journal of Guidance, Control, and Dynamics*, Vol. 39, No. 6, 2016, pp. 1173–1187.
https://doi.org/10.2514/1.G001631

[15] Ventura, J., Ciarcià, M., Romano, M., and Ulrich, W., "Fast and Near-Optimal Guidance for Docking to Uncontrolled Spacecraft," *Journal of Guidance, Control, and Dynamics*, Vol. 40, No. 12, 2017, pp. 3138–3154.
https://doi.org/10.2514/1.G001843

[16] Zagaris, C., and Romano, M., "Reachability Analysis of Planar Spacecraft Docking with Rotating Body in Close Proximity," *Journal of Guidance, Control, and Dynamics*, Vol. 41, No. 6, 2018, pp. 1416–1422.
https://doi.org/10.2514/1.G003389

[17] Dong, H., Hu, Q., and Akella, M. R., "Safety Control for Spacecraft Autonomous Rendezvous and Docking Under Motion Constraints," *Journal of Guidance, Control, and Dynamics*, Vol. 40, No. 7, 2017, pp. 1680–1692.
https://doi.org/10.2514/1.G002322

[18] Kristiansen, R., Nicklasson, P. J., and Gravdahlb, J. T., "Spacecraft Coordination Control in 6DOF: Integrator Backstepping vs Passivity-Based Control," *Automatica*, Vol. 44, No. 11, 2008, pp. 2896–2901.
https://doi.org/10.1016/j.automatica.2008.04.019

[19] Sun, L., and Huo, W., "6-DOF Integrated Adaptive Backstepping Control for Spacecraft Proximity Operations," *IEEE Transactions on Aerospace and Electronic Systems*, Vol. 51, No. 3, 2015, pp. 2433–2443.
https://doi.org/10.1109/TAES.2015.140339

[20] Sun, L., Huo, W., and Jiao, Z., "Robust Nonlinear Adaptive Relative Pose Control for Cooperative Spacecraft During Rendezvous and Proximity Operations," *IEEE Transactions on Control Systems Technology*, Vol. 25, No. 5, 2017, pp. 1840–1847.
https://doi.org/10.1109/TCST.2016.2618907

[21] Zou, A.-M., and Kumar, K. D., "Distributed Attitude Coordination Control for Spacecraft Formation Flying," *IEEE Transactions on Aerospace and Electronic Systems*, Vol. 48, No. 2, 2012, pp. 1329–1346.
https://doi.org/10.1109/TAES.2012.6178065

[22] Wang, J., Liang, H., Sun, Z., Zhang, S., and Liu, M., "Finite-Time Control for Spacecraft Formation with Dual-Number-Based Description," *Journal of Guidance, Control, and Dynamics*, Vol. 35, No. 3, 2012, pp. 950–962.
https://doi.org/10.2514/1.54277

[23] Wang, J., and Sun, Z., "6-DOF Robust Adaptive Terminal Sliding Mode Control for Spacecraft Formation Flying," *Acta Astronautica*, Vol. 73, April–May 2012, pp. 76–87.
https://doi.org/10.1016/j.actaastro.2011.12.005

[24] Filipe, N., and Tsiotras, P., "Adaptive Position and Attitude-Tracking Controller for Satellite Proximity Operations Using Dual Quaternions," *Journal of Guidance, Control, and Dynamics*, Vol. 38, No. 4, 2014, pp. 566–577.
https://doi.org/10.2514/1.G000054

[25] Lee, U., and Mesbahi, M., "Dual Quaternion Based Spacecraft Rendezvous with Rotational and Translational Field of View Constraints," *AIAA/AAS Astrodynamics Specialist Conference*, AIAA Paper 2014-4362, 2014.
https://doi.org/10.2514/6.2014-4362

[26] Dong, H., Hu, Q., and Akella, M. R., "Dual-Quaternion-Based Spacecraft Autonomous Rendezvous and Docking Under Six-Degree-of-Freedom Motion Constraints," *Journal of Guidance, Control, and Dynamics*, Vol. 41, No. 5, 2018, pp. 1150–1162.
https://doi.org/10.2514/1.G003094

[27] Gui, H., and Vukovich, G., "Finite-Time Output-Feedback Position and Attitude Tracking of a Rigid Body," *Automatica*, Vol. 74, Dec. 2016, pp. 270–278.
https://doi.org/10.1016/j.automatica.2016.08.003

[28] Filipe, N., Valverde, A., and Tsiotras, P., "Pose Tracking Without Linear- and Angular-Velocity Feedback Using Dual Quaternions," *IEEE Transactions on Aerospace and Electronic Systems*, Vol. 52, No. 1, 2016, pp. 411–422.
https://doi.org/10.1109/TAES.2015.150046

[29] Dong, H., Hu, Q., Friswell, M. I., and Ma, G., "Dual-Quaternion-Based Fault-Tolerant Control for Spacecraft Tracking with Finite-Time Convergence," *IEEE Transactions on Control Systems Technology*, Vol. 25, No. 4, 2017, pp. 1231–1242.
https://doi.org/10.1109/TCST.2016.2603070

[30] Gui, H., and de Ruiter, A. H. J., "Adaptive Fault-Tolerant Spacecraft Pose Tracking with Control Allocation," *IEEE Transactions on Control Systems Technology*, Vol. 27, No. 2, 2019, pp. 479–494.
https://doi.org/10.1109/TCST.2017.2771374

[31] Gui, H., and Vukovich, G., "Dual-Quaternion-Based Adaptive Motion Tracking of Spacecraft with Reduced Control Effort," *Nonlinear Dynamics*, Vol. 83, Nos. 1–2, 2016, pp. 597–614.
https://doi.org/10.1007/s11071-015-2350-4

[32] Udwadia, F. E., and Kalaba, R. E., *Analytical Dynamics: A New Approach*, Cambridge Univ. Press, New York, 1996, pp. 71–103.
https://doi.org/10.1017/CBO9780511665479

[33] Udwadia, F. E., and Schutte, A. D., "A Unified Approach to Rigid Body Rotational Dynamics and Control," *Proceedings of the Royal Society*, Vol. 468, No. 2138, 2011, pp. 395–414.
https://doi.org/10.1098/rspa.2011.0233

[34] Koganti, P. B., and Udwadia, F. E., "Dynamics and Precision Control of Tumbling Multibody Systems," *Journal of Guidance, Control, and Dynamics*, Vol. 40, No. 3, 2017, pp. 584–602.
https://doi.org/10.2514/1.G000633

[35] Udwadia, F., and Schutte, A., "An Alternative Derivation of the Quaternion Equations of Motion for Rigid-Body Rotational Dynamics," *Journal of Applied Mechanics*, Vol. 77, No. 4, 2010, Paper 044505.
https://doi.org/10.1115/1.4000917

[36] Udwadia, F. E., Wanichanon, T., and Cho, H., "Methodology for Satellite Formation-Keeping in the Presence of System Uncertainties," *Journal of Guidance, Control, and Dynamics*, Vol. 37, No. 5, 2014, pp. 1611–1624.
https://doi.org/10.2514/1.G000317

[37] Pothen, A. A., and Ulrich, S., "Close-Range Rendezvous of Multiple Chasers with a Moving Target Using Udwadia-Kalaba Equation," *American Control Conference*, IEEE Publ., Piscataway, NJ, 2019, pp. 3267–3272.
https://doi.org/10.23919/ACC.2019.8815115

[38] Hovell, K., "Detumbling Space Debris Using Tethers," Master's Thesis, Carleton Univ., Ottawa, 2017, pp. 35–39.
https://doi.org/10.22215/etd/2017-11870

Downloaded by CARLETON UNIVERSITY on January 23, 2022 | http://arc.aiaa.org | DOI: 10.2514/1.G005169